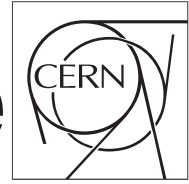


The Compact Muon Solenoid Experiment

# CMS Draft Note

Mailing address: CMS CERN, CH-1211 GENEVA 23, Switzerland



2016/03/16

Head Id: 328784

Archive Id: 333708:333861

Archive Date: 2016/02/29

Archive Tag: trunk

## Search for dark matter in monophoton final state at 13 TeV (Common AN)

A. Askew<sup>1</sup>, B. Allen<sup>2</sup>, S. Bhattacharya<sup>3</sup>, J. Buchanan<sup>5</sup>, S. Chauhan<sup>4</sup>, S. Dasu<sup>5</sup>, S. Ghosh<sup>3</sup>, B. Gomber<sup>5</sup>, Y. Iiyama<sup>2</sup>, C. Paus<sup>2</sup>, T. Perry<sup>5</sup>, A. Roy<sup>3</sup>, and M. Tripathi<sup>4</sup>

<sup>1</sup> Florida State University

<sup>2</sup> Massachusetts Institute of Technology

<sup>3</sup> Saha Institute of Nuclear Physics

<sup>4</sup> University of California at Davis

<sup>5</sup> University of Wisconsin-Madison

### Abstract

We present a search for new physics in events with one photon and large missing transverse momentum in  $2.24 \text{ fb}^{-1}$  of pp collision data at  $\sqrt{s} = 13 \text{ TeV}$  recorded in 2015.

This box is only visible in draft mode. Please make sure the values below make sense.

PDFAuthor: B. Allen, Y. Iiyama, B. Gomber

PDFTitle: Search for dark matter in monophoton final state at 13 TeV "(Common AN")

PDFSubject: CMS

PDFKeywords: CMS, physics, software, computing

Please also verify that the abstract does not use any user defined symbols



# 1 Introduction

The final states of particle collisions that involve a high-energy photon and large missing momentum is an effective probe into new physics phenomena, such as production of gravitons under models with large extra dimensions [1] or of dark matter particles [? ]. In this note, we present a search for new physics in events with one photon ( $\gamma$ ) and missing transverse momentum ( $E_T^{\text{miss}}$ ) using pp collision data at  $\sqrt{s} = 13$  TeV collected by the CMS experiment in 2015.

Large extra dimension model of the universe was proposed by Arkani-Hamed, Dimopoulos, and Dvali (ADD) in 1998 [1]. The model is motivated by the hierarchy problem, which is a theoretical peculiarity that there seem to exist two widely different fundamental length scales of nature: the electroweak scale ( $M_{EW} \sim 10^3$  GeV), at which the electromagnetic and weak interaction unify, and the Planck scale ( $M_{Pl} \sim 10^{19}$  GeV), at which gravity becomes as strong as the gauge interactions. In the ADD framework, the electroweak scale is the only fundamental length scale of the universe where gravitational and gauge interactions both unify. The model predicts that the space-time is  $\mathbb{R}^4 \times M_n$ , where  $M_n$  is a compact manifold of dimension  $n$  and volume  $R^n$ . If the gravity acts in all dimensions, the observed weakness of gravity (or, equivalently, the large value of the Planck scale) can be explained as a consequence of the universe having “large” ( $\sim$  mm) extra dimensions.

In a  $\mathbb{R}^4 \times M_n$  universe, gravitational potential  $V(r)$  between two particles of masses  $m_1$  and  $m_2$  separated by a distance  $r \gg R$  would have a form of

$$V(r) \sim \frac{m_1 m_2}{M_D^{n+2} R^n} \frac{1}{r} \quad (1)$$

because of the compactness of the extra dimensions. Parameter  $M_D$  is the true Planck’s constant in the model. Combined with Newton’s law, Eq. (1) gives the observed Planck’s constant in four dimensions:

$$M_{Pl}^2 = M_D^{n+2} R^n. \quad (2)$$

Assuming  $M_D \sim M_{EW}$ , the observed large value of  $M_{Pl}$  is obtained if  $R$  is sufficiently large for a given  $n$ . The free parameters of the model are therefore  $M_D$  and  $n$ .

The ADD model predicts observable signatures at the LHC, such as the direct production of a graviton in association with a gauge boson, which can be a photon. Gravitons produced in this way appear as Kaluza-Klein (KK) modes in  $n$  dimensions, and their momenta in the extra dimensions appear as observed mass in 4 dimensions. For large extra dimensions, the graviton mass spectrum is nearly continuous, which leads to an observed LHC signature of high- $p_T$  photon and large missing transverse momentum ( $E_T^{\text{miss}}$ ), with no specific energy scale.

The production of dark matter (DM), which dominates the matter density of the universe, is also an interesting process to look for at the LHC. In collider searches of the DM, one would typically exploit a high-energy initial-state radiation (ISR) from the incoming quarks that annihilate and produce the DM particles, since the DM particles themselves would be unobservable. When the ISR is a photon, the observed signature is again  $\gamma + E_T^{\text{miss}}$ .

Previously, effective field theories (EFT) were employed to interpret the results of  $\gamma + E_T^{\text{miss}}$  search in the context of DM production. Due to heightened general interest in the search for DM, a guideline was published by the CMS-ATLAS Dark matter forum group [2], where use of

simplified models instead of EFTs was recommended where applicable. The recommendation established a well defined set of benchmarks that enable channel combinations and allow for recasting of dark matter models against direct detection and indirect detection.

In the standard model (SM), the only process that results in a genuine signature of single photon and large  $E_T^{\text{miss}}$  is the  $Z + \gamma$  production, where the  $Z$  boson decays into a neutrino ( $\nu$ ) and an antineutrino ( $\bar{\nu}$ ). The rate of  $Z + \gamma$  production can be precisely calculable under the SM, and therefore a deviation of the observation from the prediction in this signature is a robust indication of the physics beyond the standard model. In reality, multiple other collision and non-collision processes mimic the signature and thus constitute additional background of the search. The analysis employs a series of event selections that is aimed at reducing the contributions from such non- $Z + \gamma$  background. Number of residual background events is then estimated by data-driven techniques and Monte Carlo (MC) simulations.

The CMS experiment has performed a similar search using the LHC run 1 data [? ]. No evidence of new physics in this search channel has been observed so far. The current model-independent cross section upper limit for the production of new-physics monophoton final state is 13 fb for a photon transverse momentum of 145 GeV and  $E_T^{\text{miss}}$  of 140 GeV.

## 2 Datasets

### 2.1 Data sample

We select events from AOD datasets reconstructed in CMSSW 7.4. The data sets used in this analysis are listed in 1.

Data Samples
/SinglePhoton/Run2015D-PromptReco-v3,4/AOD
/SingleElectron/Run2015D-PromptReco-v3,4/AOD
/SingleMuon/Run2015D-PromptReco-v3,4/AOD
/JetHT/Run2015D-PromptReco-v4/AOD

Table 1: List of data sets used in this analysis.

Candidate events are selected out of the SinglePhoton data set, while the remaining three data sets are used for various controls and efficiency measurements. The “golden JSON” file Cert.246908-260627.13TeV.PromptReco.Collisions15.25ns.JSON.v2.txt is used with the SinglePhoton, SingleElectron, and SingleMuon data sets to select the parts of data certified to be good for physics analysis. Corresponding recorded integrated luminosity is  $2.32 \pm 0.06 \text{ fb}^{-1}$ . For the JetHT data set, the “silver JSON” file Cert.246908-260627.13TeV.PromptReco.Collisions15.25ns.JSON.Silver.v1.txt was employed, where the recorded integrated luminosity corresponding to the sample is  $1.62 \text{ fb}^{-1}$ .

### 2.2 Monte Carlo samples

Monte Carlo (MC) event generators are used to simulate signal and background samples in order to optimize the event selection, evaluate efficiencies and systematic uncertainties, and compute expected yields. A detailed list of the simulated samples used for signal and background processes is shown in 2.

All samples are generated at leading order (LO) in QCD. For  $Z + \gamma$ ,  $W + \gamma$ ,  $\gamma + \text{jets}$ , and  $t\bar{t} + \gamma$  sample, extra colored partons are generated together with the primary process to simulate the kinematics of high-energy events better. The default set of parton distribution functions (PDFs) used to produce these samples is NNPDF3.0 [3]. For all processes, the detector response is

Process	Sample Name
Dark Matter	DarkMatter_MonoPhoton_*.13TeV-madgraph/RunIIISpring15DR74-Asympt25ns.MCRUN2.74.V9.v1/AODSIM
ADD	ADDmonoPhoton_MD-.*_d-.*_TuneCUETP8M1.13TeV-pythia8/RunIIISpring15DR74-Asympt25ns.MCRUN2.74.V9-v/AODSIM
$Z(\rightarrow \nu\nu) + \gamma$	ZNuNuGJets_MonoPhoton_PtG-130.TuneCUETP8M1.13TeV-madgraph/RunIIISpring15DR74-Asympt25ns.MCRUN2.74.V9.v1/AODSIM
$Z(\rightarrow \ell\ell) + \gamma$	ZLLGJets_MonoPhoton_PtG-130.TuneCUETP8M1.13TeV-madgraph/RunIIISpring15DR74-Asympt25ns.MCRUN2.74.V9.v1/AODSIM
$W(\rightarrow \ell\nu) + \gamma$	WGJets_MonoPhoton_PtG-130.TuneCUETP8M1.13TeV-madgraph/RunIIISpring15DR74-Asympt25ns.MCRUN2.74.V9.v1/AODSIM
$W(\rightarrow e\nu)$	WToENu_M-100.TuneCUETP8M1.13TeV-pythia8/RunIIISpring15DR74-Asympt25ns.MCRUN2.74.V9.v2/AODSIM
$W(\rightarrow \mu\nu)$	WToMuNu_M-100.TuneCUETP8M1.13TeV-pythia8/RunIIISpring15DR74-Asympt25ns.MCRUN2.74.V9.v1/AODSIM
$W(\rightarrow \tau\nu)$	WToTauNu_M-100.TuneCUETP8M1.13TeV-pythia8-tauola/RunIIISpring15DR74-Asympt25ns.MCRUN2.74.V9.v2/AODSIM
$\gamma + \text{jets}$	GJets_HT-.TuneCUETP8M1.13TeV-madgraphMLM-pythia8/RunIIISpring15DR74-Asympt25ns.MCRUN2.74.V9.v*/AODSIM
$t\bar{t} + \gamma$	TTGJets_TuneCUETP8M1.13TeV-amcatnloFXFX-madspin-pythia8/RunIIISpring15DR74-Asympt25ns.MCRUN2.74.V9.v1/AODSIM
QCD	QCD_Pt.EMEnriched.TuneCUETP8M1.13TeV-pythia8/RunIIISpring15DR74-Asympt25ns.MCRUN2.74.V9-v/AODSIM

Table 2: List of the simulated samples used for signal and background processes.

simulated using a detailed description of the CMS detector, based on the GEANT4 package [4]. Minimum bias events are superimposed on the simulated events to emulate the additional pp interactions per bunch crossing (pile-up). These samples are re-weighted to represent the pile-up distribution as measured in the data.

The background processes listed in 2 could mimic the  $\gamma + \cancel{E}_T$  final state in the following ways:

- $Z(\rightarrow \nu\nu) + \gamma$  is the irreducible background as it has the same final state.
- $W(\rightarrow \ell\nu) + \gamma$  in which the charged lepton is lost or misreconstructed.
- Inclusive  $W(\rightarrow \ell\nu)$  production where the lepton fakes a photon.
- $Z(\rightarrow \ell\ell) + \gamma$  in which both leptons are lost or misreconstructed.
- $t\bar{t} + \gamma$  where  $t\bar{t}$  undergoes a (semi)leptonic decay, and the charged lepton is lost or misreconstructed.
- Other  $\gamma + X$  events in which the  $E_T^{\text{miss}}$  is mismeasured.

### 3 Event Selection

The signal candidate events are collected by the trigger HLT\_Photon165\_HE10\_v\*. The following recommended noise event filters recommended by JetMET POG are applied on data:

- CSC beam halo filter : To reject beam halo muons.
- HBHE noise filter : To reject noisy HCAL events.
- HBHE noise filter with isolated noise rejection : To reject noisy HCAL events.
- EE badSC noise filter : Removing events from two EE crystals giving anomalous high energies.
- ECAL TP filter : Reject events where masked crystals produce large missing energy.

Events are also required to have at least one good reconstructed vertex with  $N_{\text{d.o.f.}} > 4$ ,  $|z| < 24$  cm, and  $\rho < 2$  cm with respect to the origin of the CMS coordinate.

After selecting a good vertex, we require at least one photon object with  $E_T > 175$  GeV. The photon is also required to be in the barrel fiducial region of the detector ( $|\eta| < 1.4442$ ).

The choice of using only the barrel photons is based on two considerations. The first is that the signal events tend to produce more central photons than forward ones, as demonstrated in Fig. 1. The second point is that, as described in detail in Sec. 5.6, the default method of estimating the beam halo background breaks down for endcap photons.

Two of the background sources to single-photon event selection are the misidentification of jets and electrons as photons. A jet can be misidentified as a photon when a neutral particle such as  $\pi^0$  (or  $\eta$ ) within the jet carries a significant fraction of the  $p_T$  and the photons from its subse-

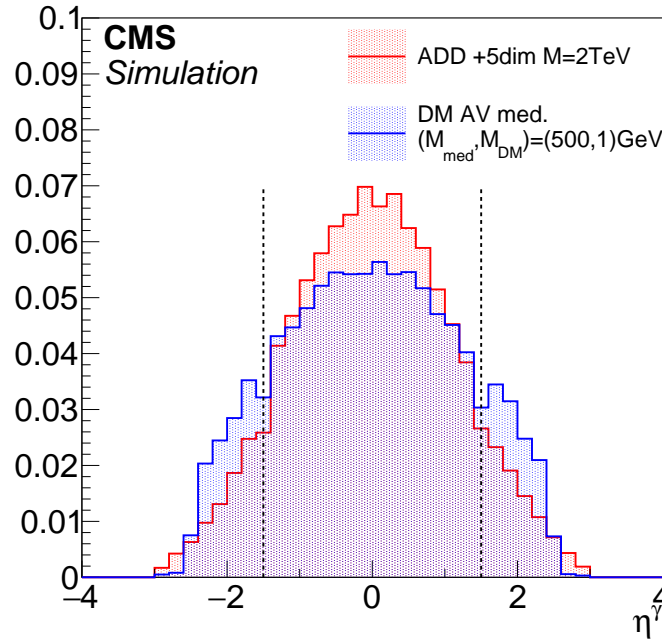


Figure 1:  $\eta$  distributions of photons from two signal model points.

quent decay are collimated such that they appear as a single photon in ECAL. Electrons may be misreconstructed as photons due to inefficiency in the track reconstruction. To minimize these contributions, requirements are placed on the isolation variables, shower width, and pixel seed match calculated for the photon based on medium Photon ID [5]. These requirements are:

- **Particle Flow Photon Isolation ( $I_{\text{Ph}}$ ):** Sum of  $E_T$  of all PF photons which are not in the “footprint” of the candidate photon and are within a cone of  $\Delta R = 0.3$  is required to be less than  $(0.28 + 0.0053 \times (E_T^\gamma / \text{GeV})) \text{ GeV}$ , after correcting the sum for pileup using Fastjet  $\rho$  and the effective area computed by the EGM POG.
- **Particle Flow Charged Isolation ( $I_{\text{CH}}$ ):** Sum of  $p_T$  of all PF charged hadrons which are associated to the primary vertex, not in the “footprint” of the candidate photon, and within a cone of  $\Delta R = 0.3$  is required to be less than 1.37 GeV.
- **Particle Flow Neutral Isolation ( $I_{\text{NH}}$ ):** Sum of  $E_T$  of all PF neutral hadrons which are not in the “footprint” of the candidate photon and are within a cone of  $\Delta R = 0.3$  is required to be less than  $(1.06 + 0.014 \times (E_T^\gamma / \text{GeV}) + 0.000019 \times (E_T^\gamma / \text{GeV})^2) \text{ GeV}$ , after correcting the sum for pileup using Fastjet  $\rho$  and the effective area computed by the EGM POG.
- **Single tower H/E :** Ratio of the energy deposited in the single closest HCAL tower to the supercluster position and the energy deposited in ECAL to that supercluster is required to be less than 0.05.
- $\sigma_{i\eta i\eta}$ : The width of the shower in  $i\eta$ -space is required be less then 0.0102 . This variable characterizes the shape of the electromagnetic shower.
- **Pixel seed:** To minimize the contribution from misidentified electrons, the photon is required not to have an associated pixel seed.

The PF-based charged isolation of the photon is computed using the primary vertex (PV), because the high- $E_T$  photon we consider is assumed to emerge from the hard scattering at the



PV. The PV is the vertex with the highest  $\sum p_T^2$ . The actual rate that the photon comes from the PV depends on the pileup activity in the event. For a  $\gamma + E_T^{\text{miss}}$  final state in a high pileup environment, a significant fraction of the event may have the photon not originating from the PV, because it is often the case that the hard-scattering vertex has little charged track activity. Misassignment of the photon vertex leads to an artificially smaller value of isolation. Thus, an additional PF-based charged isolation is computed in the same manner and with same cone size, but with respect to all vertices in the event. The largest of such isolation sums ("PF Worst Charged Hadron Isolation ( $I_{\text{WCH}}$ )") is then used in place of the PV-based PF charged isolation, thus ensuring in a conservative way that this electromagnetic object is indeed isolated from charged hadron activity. Naively, one can simply replace  $I_{\text{CH}}$  with  $I_{\text{WCH}}$  in the event selection. However, doing so would introduce undesired pileup dependency of the isolation efficiency, and therefore  $I_{\text{WCH}}$  must be further corrected using Fastjet  $\rho$  and effective areas measured specifically for this analysis. Details of the computation of the effective areas are given in Appendix A.

Since the non-collision processes such as cosmics, beam halo, and anomalous calorimeter signals can all appear as  $\gamma + E_T^{\text{miss}}$  events, further requirements are imposed on the candidate photon object:

- Spike veto:

- $\sigma_{i\eta i\eta} > 0.001$
- $\sigma_{i\phi i\phi} > 0.001$

Showers narrower than the above thresholds in  $\eta$  or  $\phi$  directions are unphysical for genuine photons. These requirements reduce the small contribution from ECAL spikes that pass the multiple levels of spike-cleaning applied through the trigger and reconstruction processes.

- Cosmics/Halo veto:

- Seed crystal time is required to be within  $\pm 3$  ns of that of an ideal prompt shower.
- MIP total energy is required to be less than 4.9 GeV.

MIP total energy is computed by summing up additional ECAL energy deposits consistent with potential paths of the beam halo minimum-ionizing particle (MIP) that penetrates the ECAL.

The missing transverse momentum present in the event is computed as the negative sum of the transverse momentum of all particle flow candidates in the event. Type-1 correction as defined by the JetMET POG is applied to improve the  $E_T^{\text{miss}}$  scale and resolution. Summer15\_25nsV6 jet energy scales are used for the correction. Events are required to have  $E_T^{\text{miss}} > 170$  GeV. Because the photon candidate is expected to be recoiling against the missing new physics particle in the signal events,  $E_T^{\text{miss}}$  and photon are required to be separated by more than 2 radians in the azimuthal angle.  $E_T^{\text{miss}}$  threshold of 170 GeV is derived using an ADD signal model point by maximizing the ratio of the signal yield to the square root of the expected background. More details are given in Appendix B.

Electrons and muons are identified in the event with the loose criteria defined by the EGM and MUO POGs. Events with electrons or muons with  $p_T > 10$  GeV that are farther away from the candidate photon by  $\Delta R > 0.5$  are vetoed to minimize the contribution from  $W\gamma$ .

Jets are also used for event veto purposes. Jets are reconstructed by clustering the particle flow candidates through the anti- $k_T$  algorithm with a distance parameter of  $R = 0.4$ . All

neutral candidates and charged candidates associated to the primary vertex are included in the clustering. Jet momenta are corrected with Summer15\_25nsV6 calibration constants. Jets with corrected  $p_T > 30$  GeV and  $|\eta| < 5.0$  are considered, if they are farther away from the candidate photon by  $\Delta R > 0.4$ .

An event is rejected if the azimuthal opening angle between the missing transverse momentum and the closest jet ( $\min \Delta\phi(\text{jet}, E_T^{\text{miss}})$ ) is less than 0.5 radians. Only up to four leading jets are considered in  $\min \Delta\phi(\text{jet}, E_T^{\text{miss}})$ . This requirement is highly efficient in reducing the  $\gamma + \text{jets}$  background. N-1 plots for the  $\min \Delta\phi(\text{jet}, E_T^{\text{miss}})$  and  $\Delta\phi(\text{pho}, E_T^{\text{miss}})$  are shown in Fig. 2.

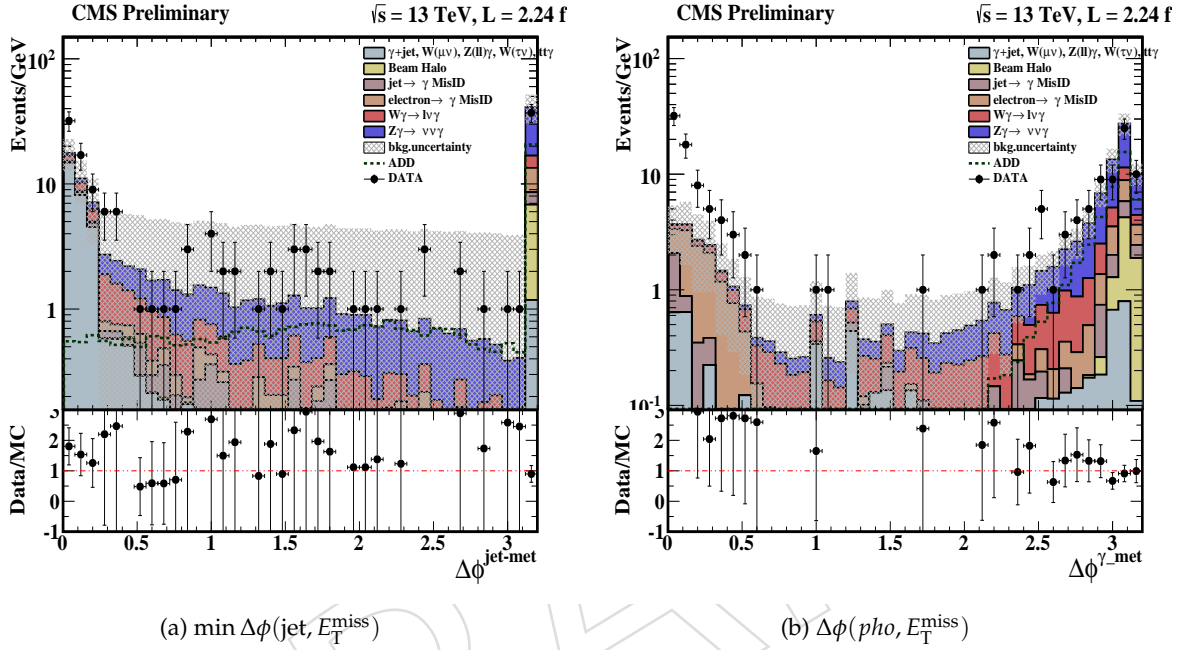


Figure 2: The  $\min \Delta\phi(\text{jet}, E_T^{\text{miss}})$  and  $\Delta\phi(\text{pho}, E_T^{\text{miss}})$  N-1 distribution for the candidate sample, compared with estimated contributions from SM backgrounds, and background uncertainty includes statistical and systematic error.

The selection cut flow table for ADD signal is shown in shown in Tab. 3

Selection criteria	ADD Signal
Initial events	351006
Good photon with $p_T > 175$ GeV	66399
$E_T^{\text{miss}} > 170$ GeV	34294
$\Delta\phi(\gamma, E_T^{\text{miss}}) > 2$	34295
Lepton veto	32289
$\min \Delta\phi(\text{jet}, E_T^{\text{miss}})$	28758

Table 3: A cut flow table for an ADD signal model.

## 4 Efficiencies and Scale Factors

### 4.1 Trigger efficiency

The efficiency of the main single-photon trigger is measured in data. While the trigger is seeded by L1SingleEG30, the offline photon  $E_T$  threshold is 175 GeV. Therefore we assume that the full



L1 efficiency has been attained well before our successive cuts. Thus our main concern is to determine the turn-on curve of the HLT conditions with respect to offline selection.

To measure the efficiency, we select events passing prescaled triggers with lower  $E_T$  thresholds, namely HLT\_Photon75\* and HLT\_Photon90\* and HLT\_Photon120\*. We apply our analysis selection requirements on the events firing these triggers, and compute the rate at which such events have also fired the main analysis trigger. The relative trigger efficiency measured in this way is shown in Fig. 3.

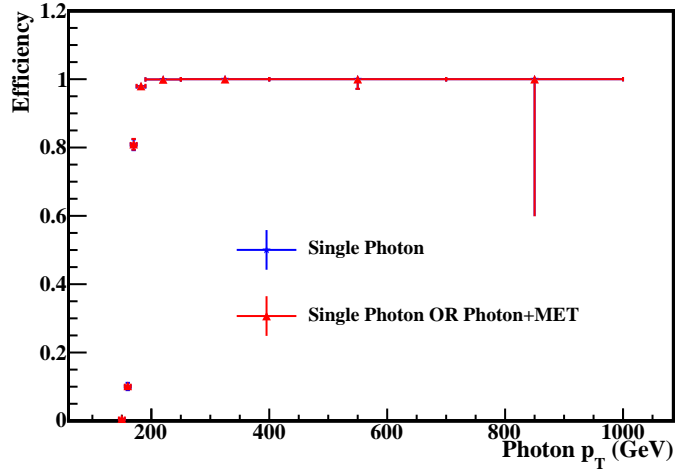


Figure 3: Relative trigger efficiency for the single photon triggers and OR of single photon and photon+MET trigger as a function of offline photon candidate transverse momentum.

One can see that the triggers become fully efficient (98%) in the range of approximately 175 GeV.

As a potential trigger requirement, we considered combining the single-photon trigger with a photon plus  $E_T^{\text{miss}}$  trigger to achieve a higher trigger efficiency. However, as demonstrated in Fig. 3, there is very little gain in efficiency from the combination. Considering the complication a combined trigger would introduce, a choice was made to rely on the single-photon trigger only.

## 4.2 Absolute trigger efficiency using JetHT data set

The HLT trigger efficiency was suspected to be biased due to the presence of additional HE10 and NoHE cut in the triggers used in the numerator of trigger efficiency. To check the effect of these requirements, we measure the absolute *unprescaled* single photon trigger efficiency as a function of  $E_T^\gamma$  using the JetHT dataset which utilizes criteria mostly orthogonal to the single photon trigger requirements.

The trigger efficiency has been calculated in the same way as described in Sec. 4.1 but with different triggers in the denominator. The list of triggers used in the denominator are HLT\_Jet60, HLT\_Jet80, and HLT\_Jet140. The corresponding trigger efficiency is shown in 4. The single photon triggers are fully efficient above the offline cut of  $E_T^\gamma > 175$  GeV.

## 4.3 MIP veto

We decided on the value of the MIP cut based on the efficiency and rejection using two data samples: in-time halo which was tagged using the CSCHalo filter and  $W \rightarrow e\nu$  events which were in time. Figure 5 shows the ROC curve, and the efficiency versus cut curves for this

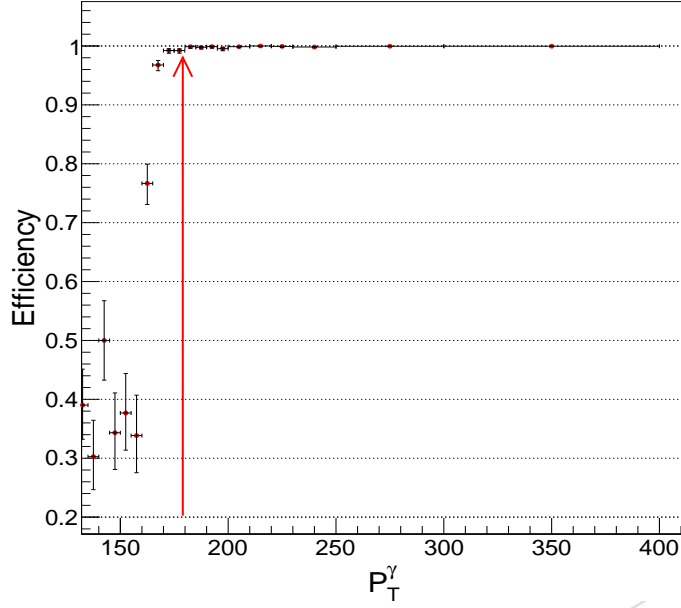


Figure 4: Absolute trigger efficiency for Single photon trigger as a function of photon  $p_T$ .

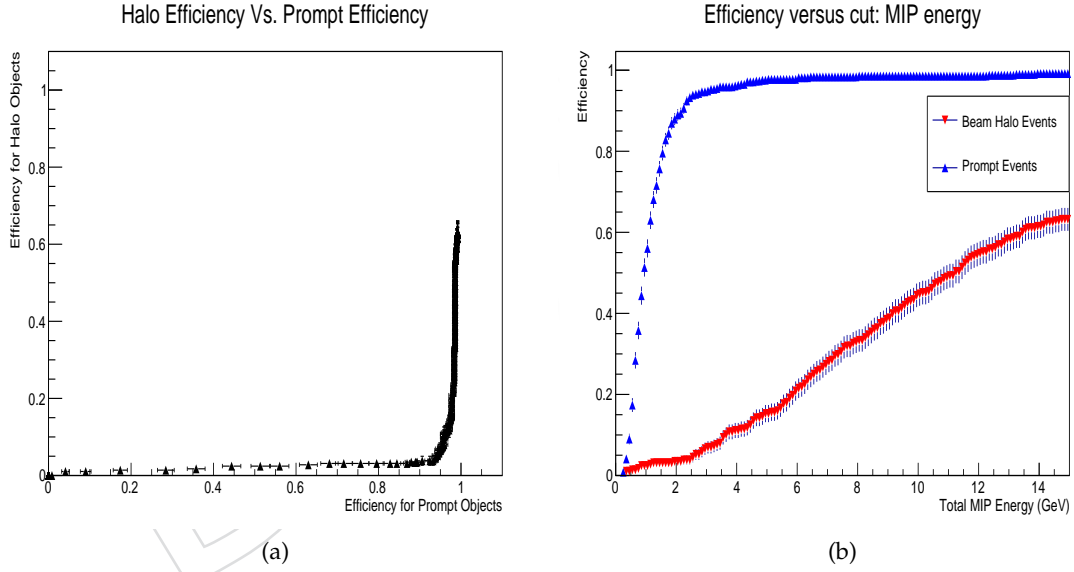


Figure 5: ROC curve and the efficiency versus cut curves for the MIP total energy

variable using these two samples. If we simply look at these figures, we find that we are not actually cutting very hard, and in principle we could cut harder. In the left plot, the red curve is for beam halo events which was tagged using the CSCHalo filter and blue curve represents  $W \rightarrow e\nu$  prompt events. At the cut value of 4.9 GeV, prompt efficiency is 0.95 and beam halo efficiency is 0.20.

#### 4.4 Photon identification efficiency scale factor

Data/MC efficiency scale factors for the photon identification at the medium working point is provided by the EGM POG, and the values for the  $E_T^\gamma$  bin relevant to this analysis are summarized in Table ???. The values in the table include the scale factor of the pixel veto efficiency, also

Efficiency	$W_{\text{ev}}$ MC	$W_{\text{ev}}$ Data
Lepton Veto	$0.99 \pm 0.05$	$0.95 \pm 0.06$

Table 4: N-1 efficiencies.

Efficiency	$Z\mu\mu\gamma$ MC	$Z\mu\mu\gamma$ Data
PFWorst Charged Hadron Isolation and MIP total energy	$0.87 \pm 0.04$	$0.87 \pm 0.06$

Table 5: N-1 efficiencies.

provided by the EGM POG, of  $1.01 \pm 0.024$ .

$\eta$	[-1.444, -1]	[-1, 0]	[0, 1]	[1, 1.444]
$E_{\text{T}}^{\gamma} > 50 \text{ GeV}$	$1.007 \pm 0.031$	$0.992 \pm 0.027$	$0.994 \pm 0.027$	$0.997 \pm 0.031$

Table 6: N-1 efficiencies.

#### 4.5 Scale factors for $I_{\text{WCH}}$ , MIP total energy, and lepton veto

Because the common medium working point does not involve MIP tagger and  $I_{\text{WCH}}$  requirements, data/MC efficiency scale factor must be separately derived for these criteria. A combined efficiency is measured in a  $Z \rightarrow \mu\mu\gamma$  control sample in data, where a sample of pure photons are collected by requiring two muons and a photon in the event with the three-body mass consistent with  $M_Z$ . The obtained efficiency is then compared to the efficiency computed in the MC for the same final state. Efficiencies are shown in Tab. 6. Uncertainties quoted in Tab. 6 are statistical.

The lepton veto efficiency scale factor is measured by comparing dimuon events in data and MC. Events are respectively taken from SingleMuon data set and a mixture of DY,  $t\bar{t}$ , WW, WZ, and Z Z samples with a requirement of two tightly selected muons with the mass between 61 and 121 GeV. These events are then checked for additional electron or muon objects passing the loose selection criteria. The efficiency is inspected as a function of number of vertices, number of jets, and  $H_{\text{T}}$  in the event, and in all cases data and MC agreed well (Fig. 6). On the other hand, the veto efficiency in MC dimuon sample is significantly different from that of the  $Z(\rightarrow \nu\nu)\gamma$  sample, which more closely feature the properties of the signal candidate sample. The dependence of the efficiencies to  $H_{\text{T}}$  hints that the difference emerges from difference in event kinematics, but no full understanding is achieved yet. In anticipation of further developments, the full difference in the efficiencies between dimuon and  $Z\gamma$  samples is tentatively taken as the systematic uncertainty in the lepton veto scale factor, which is therefore  $1.00 \pm 0.02$ .

#### 4.6 Scale factors

A summary of the data/MC scale factors and their uncertainties is shown in Table 7. The product of the scale factors are applied to all the MC based estimates. The total uncertainty of 6% is dominantly due to statistical uncertainty in the measurement of MIP tagger and  $I_{\text{WCH}}$  efficiency scale factor.

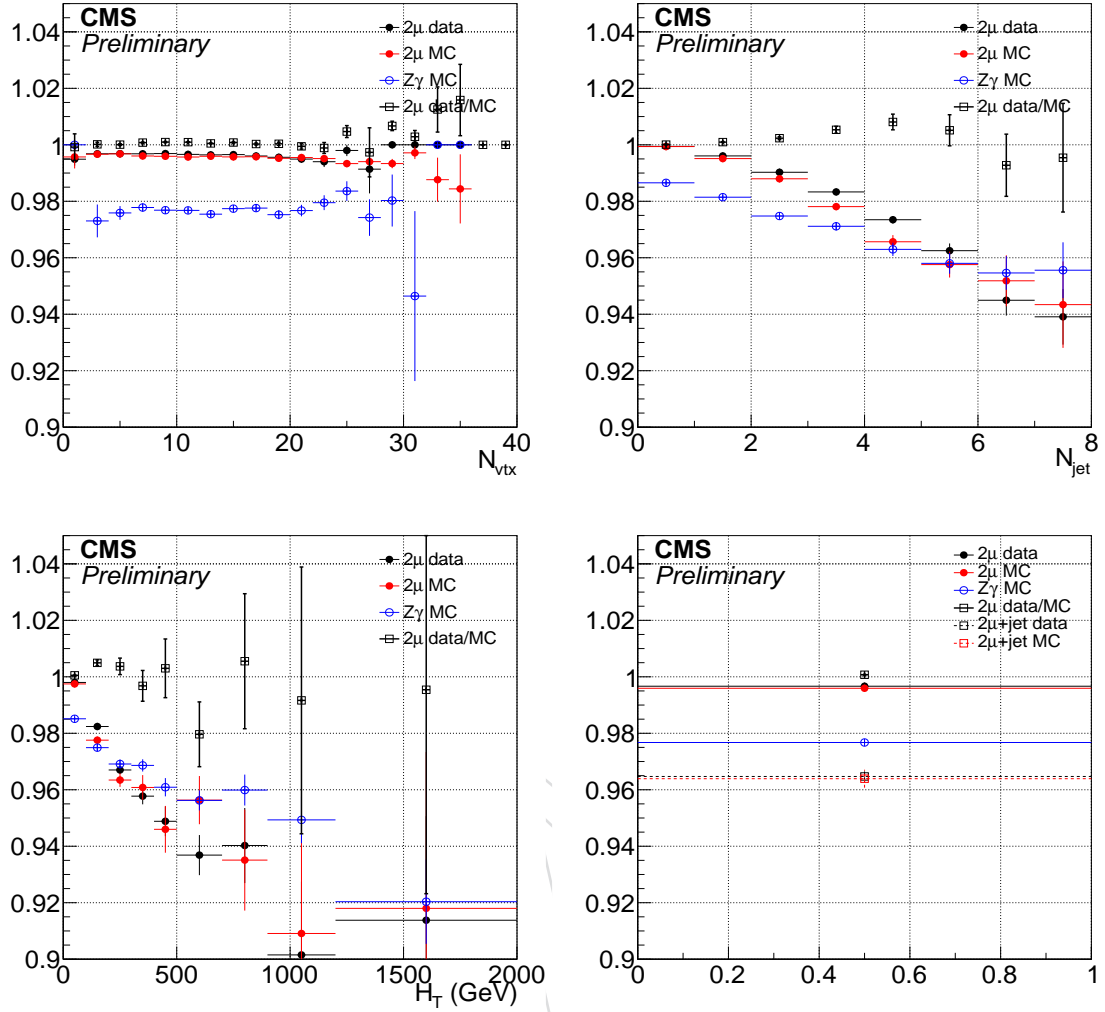


Figure 6: Lepton veto efficiencies and data/MC scale factors as functions of  $N_{\text{vtx}}$ ,  $N_{\text{jet}}$ , and  $H_T$ , and the corresponding inclusive values. While dimuon and  $Z\gamma$  samples have significantly different efficiencies, data and MC agree well within dimuon samples, giving scale factors consistent with 1 almost everywhere. This is true even when additionally requiring a high- $p_T$  jet in the event, as seen in the inclusive efficiency plot. Given these observations, it is likely that the uncertainty in the scale factor can be narrowed down significantly. However, until the different effects are understood, the difference between  $Z\gamma$  and dimuon efficiencies itself is taken as the uncertainty.

Source	Estimate for $\rho$
Photon ID	$0.99 \pm 0.016$
Pixel Seed	$1.00 \pm 0.024$
$I_{\text{WCH}}$ and MIP total energy	$1.00 \pm 0.05$
Lepton veto	$1.00 \pm 0.02$
Total	$0.99 \pm 0.06$

Table 7: Efficiency data/MC scale factors.

## 5 Background estimation

### 5.1 Overview

As mentioned in Sec. 1, there are multiple distinct sources of SM background to this analysis. The most significant of them is the so-called irreducible background, which is the production of a Z boson in association with a high-energy photon ( $Z + \gamma$ ) where the Z boson decays into a neutrino-antineutrino pair. The second leading background contribution comes from the production of a W boson in association with a high-energy photon. This type of events become a background for this analysis when the W boson decays leptonically and emits a neutrino or an antineutrino together with a charged lepton. A large fraction of such events are rejected by the electron and muon vetoes in the event selection. However, hadronic tau events and events where the leptons are out of the reconstruction acceptance will remain, and the vetoes themselves have imperfect efficiencies. These two background sources are estimated using MC simulations.

We also consider  $Z \rightarrow \ell\ell + \gamma$ ,  $t\bar{t} + \gamma$ , and  $W \rightarrow \mu\nu$  with a strong collinear radiation from the muon. These processes, collectively denoted as minor SM backgrounds, can contribute in the signal region if the leptons go out of acceptance or are not captured by the veto. The effective rate of such processes are much smaller than  $Z + \gamma$  and  $W + \gamma$ . MC simulations are also used to predict their contribution.

Less significant but non-negligible background arise from events where the candidate photon object is a misidentified electron or electromagnetic shower caused by hadrons. Such misidentifications are rare, but the processes with final states that are prone to misidentification have high cross sections. The background events from electron misidentification are mostly W boson production ( $W \rightarrow e\nu$ ), whereas those from hadron misidentification can be due to multiple sources such as  $Z(\rightarrow \nu\nu) + \text{jets}$  and QCD multijet with grossly mismeasured jet energy. Since object misidentification rates depend on subtle details of the detector, MC simulation cannot be expected to model it reliably. Therefore, data-driven techniques are employed to estimate the contributions from these background events.

Jet energy mismeasurement can also make  $\gamma + \text{jets}$  events appear to have large  $E_T^{\text{miss}}$ . However,  $E_T^{\text{miss}}$  typically aligns with one of the jets in such cases, and therefore the requirement that  $E_T^{\text{miss}}$  be separated from jets in the event reduces this background highly effectively. The residual of this background is estimated with a data-driven method.

Finally, large (real and spurious) energy deposits in ECAL from non-collision processes can mimic  $\gamma + E_T^{\text{miss}}$  events and therefore need to be controlled. Known sources of such background include bremsstrahlung of beam halo or cosmic ray muons and noise in the ECAL photodetectors and electronics. Data-driven estimations based on the pulse time of the seed ECAL hit and the azimuthal angle distribution of the showers are employed to estimate the contributions from these non-collision background events.

### 5.2 $Z\gamma$ and $W\gamma$

$Z + \gamma$  and  $W + \gamma$  background contributions are modeled and estimated using MC simulations. Samples generated at leading order (LO) in QCD by MADGRAPH 5 with up to two additional partons and a generator-level requirement of  $p_T^\gamma > 130 \text{ GeV}$  are employed. A

To correct the overall normalization, the samples are scaled to the corresponding next-to-next-to leading order (NNLO) cross sections calculated by Grazzini et al. [6] for  $p_T^\gamma > 175 \text{ GeV}$  and  $|\eta^\gamma| < 1.4442$ . For the  $Z + \gamma$  sample, the differential cross section  $d\sigma/dp_T^\gamma$  was made available,

$p_T^\gamma$ range (GeV)	$\sigma$ (fb)	NNLO / LO
<b>Z + <math>\gamma</math></b>		
[175, 190]	14.4	1.39
[190, 250]	29.7	1.35
[250, 400]	17.5	1.30
[400, 700]	3.7	1.23
[700, inf]	0.3	1.23
<b>W + <math>\gamma</math></b>		
[175, inf]	243.9	1.34

Table 8: Cross sections used to normalize the Z +  $\gamma$  and W +  $\gamma$  samples.

which enables the correction also of the slight discrepancy in the  $p_T^\gamma$  spectrum between the LO and the higher order calculations. The cross section values are summarized in Tab. 8.

Additionally, to account for rate suppression due to higher-order electroweak effects at high vector boson  $p_T$ , correction factors taken from Refs. [7] and [8] are applied to these samples as a function of photon  $p_T$ .

For the systematic uncertainty on Z +  $\gamma$  and W +  $\gamma$  estimates, four sources are considered : PDF and scale uncertainties, which are 5.37% and 8.9% respectively; electroweak correction uncertainties, where the full correction is conservatively taken as the uncertainty which is 11% for Z +  $\gamma$  and 7% for W +  $\gamma$ ; scale factor, which is 6% as mentioned in Sec. 4.6; and systematic uncertainty due to JET/MET/Photon energy scale and pileup, which is 6.2% as mentioned in next section.

### 5.3 Electron misidentification

An electron can be misidentified as a photon if the association of track seeds in the pixel detector to the supercluster in ECAL fails in the reconstruction step. The production of a single W boson decaying to an electron and a neutrino is a high-rate process, and it mimicks the photon plus  $E_T^{\text{miss}}$  signature if the electron is misidentified.

The rate at which this misidentification occurs is proportional to the inefficiency  $1 - \epsilon_e^{\text{pixel}}$  of the pixel seeding, defined over the electrons passing the photon identification criteria described in Sec. 3 except the pixel-seed veto. This partial identification is denoted as  $e\gamma$  ID in the following. If one assumes that the kinematic and other critical properties of the electron plus  $E_T^{\text{miss}}$  events are unaffected by the electron misidentification, it is possible to model the electron misidentification background by taking a proxy sample with well-identified electrons and scaling this sample by  $R_e = (1 - \epsilon_e^{\text{pixel}}) / \epsilon_e^{\text{pixel}}$ .

The factor  $R_e$  is estimated by exploiting the Z boson decay into an  $e^+e^-$  pair. In this “tag-and-probe” (TP) method, a high-quality electron object (tag) is identified in a single electron data sample, and the accompanying electron is sought for in the pool of electromagnetic objects (probes) in the event. The probes must pass the  $e\gamma$  ID. The area of the peak in the mass distribution of the tag-probe system around the Z boson mass is then measured once applying the pixel-seed veto requirement on the probe and once inverting the veto. Denoting the two areas  $N^{e\gamma}$  and  $N^{ee}$ , respectively, the ratio  $N^{e\gamma} / N^{ee}$  is equal to  $R_e$  up to minor systematic corrections.

Events collected by the single electron trigger HLT\_Ele23\_WPLoose\_Gsf in the SingleElectron data set are used for this TP measurement. The tag electron is identified through the EGM “Spring15 25ns tight” identification criteria [] and is required to match the trigger object. All



possible tag-probe combinations are considered; if the tag object can also serve as a probe and the probe object as a tag, which is a common occurrence in the case where a pixel seed is required on the probe, then the two combinations are considered independently to avoid the bias caused by somehow preferring one object over another to use as the probe.

The tag-probe mass distributions are then fit to extract  $N^{e\gamma}$  and  $N^{ee}$ . The fit model is composed of two templates, where one template describes a pure  $Z \rightarrow ee$  line shape and the other describes the background contributions. The backgrounds to the  $ee$  fit include  $W + \text{jets}$ , diboson, and  $t\bar{t}$  productions, which are all negligible and estimated to contribute by less than 1%. The backgrounds to the  $e\gamma$  fit on the other hand mainly consist of processes with actual electron and photon in the final state, such as  $W\gamma$  and  $Z \rightarrow ee$  with a hard radiation off one of the electrons.

The  $Z \rightarrow ee$  template is obtained from the DY MC sample by applying the same TP selection as above but without any trigger requirement. In order to account for the electron and photon momentum scale and resolution differences in data than in MC, the template is convoluted with the Crystall Ball function with all parameters floating in the fit.

The background template is obtained from a single muon sample, making use of the fact that the most of the background processes in both fits are symmetric in lepton flavor. Events collected with the trigger HLT\_IsoMu24\_eta2p1 from the SingleMuon dataset is subjected to a modified TP selection, where the tag is a tight muon [] matching the trigger object. In order to mitigate the statistical fluctuation in the background sample, the actual template is constructed by a Gaussian kernel estimation of the mass distribution of this muon-probe sample.

The floating parameters of the fits are therefore the normalizations of the  $Z \rightarrow ee$  and background templates and the Crystal Ball smearing parameters. Figure 7 shows the  $ee$  and  $e\gamma$  fits for TP pairs where the probe  $p_T$  is between 100 GeV and 400 GeV, from which the  $R_e$  factor used for the estimation of the electron misidentification background is derived. The  $R_e$  factor is computed as the ratio of the integral of the signal template functions in the two fits. Because the lower-mass tail of the signal template can be mismodeled by e.g. overly enhanced loss-tail parameter of the Crystal Ball function and still appear as a good fit by suppressing the background, the mass window between 81 GeV and 101 GeV is used for the nominal values of the integral.

The proxy sample for the background estimation is obtained by identical event selection as that described in Sec. 3, but with the pixel-seed veto inverted on the photon candidate object.

Systematic uncertainties in this method to estimate the electron misidentification background can be categorized to those related to the TP fit and those related to the applicability of the  $R_e$  factor. The fit uncertainty in turn includes statistical uncertainty and the potential mismodeling of the  $Z \rightarrow ee$  and background shapes.

The statistical uncertainty of the fits are estimated by generating toy data from the nominal fit result with the same number of entries as the fit target distribution. The mass distribution of the toy data is then fit with the same model with the parameters floating. This procedure is repeated 100 times to obtain a distribution of the  $Z \rightarrow ee$  event yields, and its standard deviation is taken as the statistical uncertainty of the fit. Relative statistical uncertainty on the  $R_e$  factor is 22%.

The effect of potential mismodeling in the fits is evaluated by using an alternative background shape. The fit is repeated with a first-order polynomial as the background model, and the difference in the  $Z \rightarrow ee$  event yield from the nominal fit are taken as the systematic uncertainty. The estimated relative uncertainty of this component is 14%.

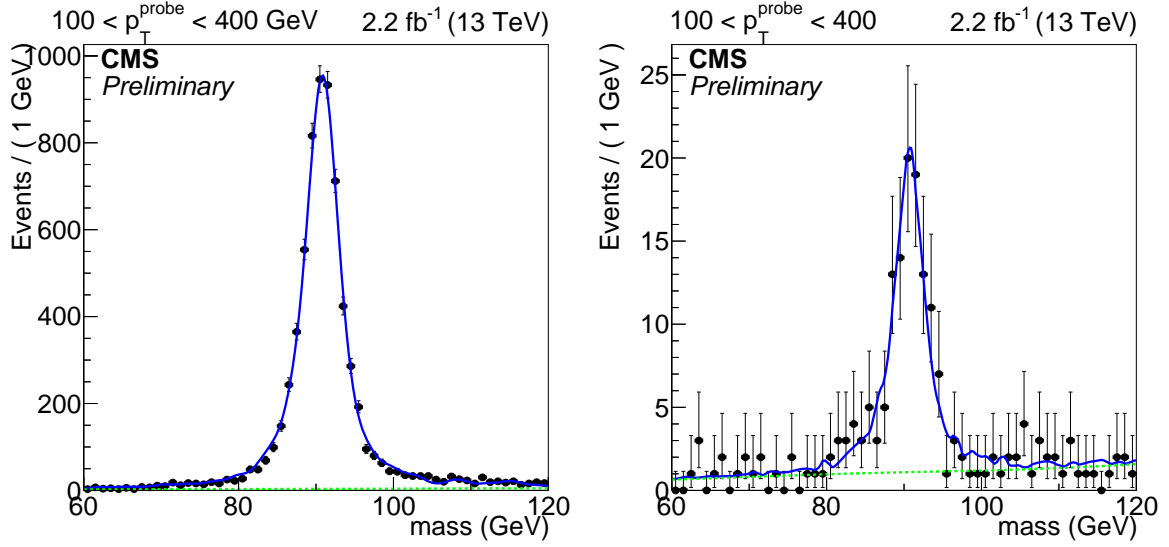


Figure 7: Fits to the mass distributions for  $ee$  (left) and  $e\gamma$  (right) selections. The blue solid line represents the full fit model, and the green dashed line its background component.

Additionally, the same measurement is performed on the mixture of DY and  $W + \text{jets}$  MC simulations to compare the fit result to the  $R_e$  factor calculated from the generator-level information. Figure 8 shows the fit result along with the MC truth information. The value of  $R_e$  obtained from the fit is 0.0066, whereas that from the MC truth information is 0.0055. The difference between the measured and calculated values however depends strongly on the radiation modeling in the DY simulation, because a big component of the background in the  $e\gamma$  fit is the hard radiation DY events. Therefore this additional uncertainty evaluation is not considered in the final result.

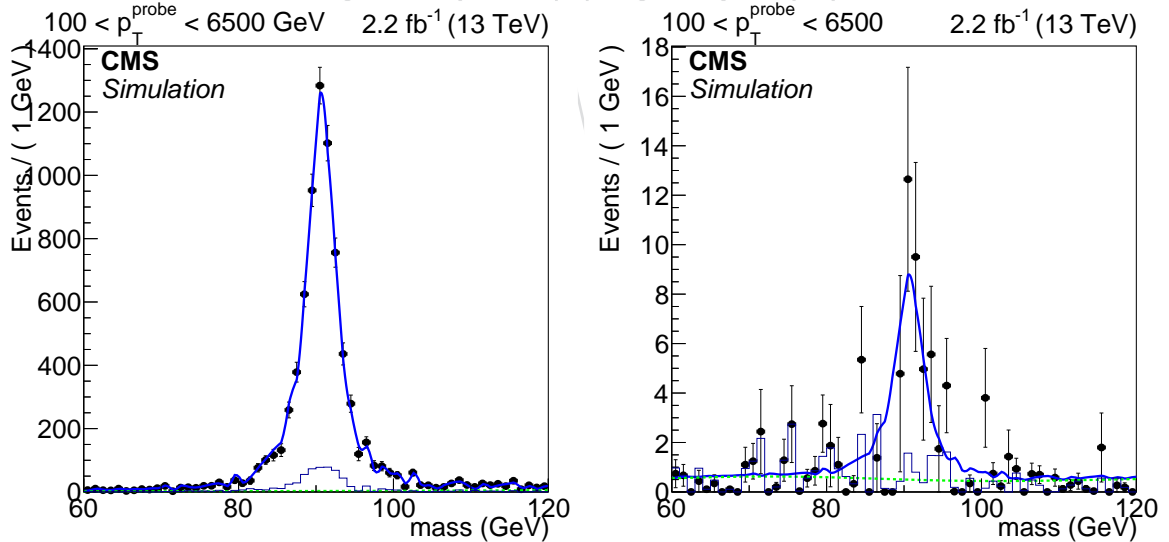


Figure 8: Fits to the mass distributions for  $ee$  (left) and  $e\gamma$  (right) selections in MC simulation. The blue thin histograms are the component of the target distribution where the probe was not matched to a generator-level electron within  $dR < 0.1$ .

Finally, the applicability of the  $R_e$  factor derived from  $Z \rightarrow ee$  events to the electron-misidentification background of this analysis, which is mainly  $W \rightarrow e\nu$ , is assessed. It has been observed in the past [9] that the correlation of  $\epsilon_e^{\text{pixel}}$  to additional uncontrolled variables causes sizeable mis-

estimation of the electron misidentification rate in processes that are not  $Z \rightarrow ee$ . One example of such variables is the number of tracks that emerge from the vertex where the misidentified electron originates. This effect can be understood by considering the fact that  $\epsilon_e^{\text{pixel}}$  is directly related to the pixel seeding efficiency of the electron. The pixel seeding efficiency is higher if the vertex has more associated tracks, since an easily identifiable vertex can be used in a 2+1 (two pixel hits plus a vertex) identification of the track seeds. Conversely, if the vertex has few tracks besides that of the electron, the seeding efficiency can be low and thus the  $\epsilon_e^{\text{pixel}}$  factor high, up to more than three times the average value. As most of the  $Z \rightarrow ee$  events with probe  $p_T > 100 \text{ GeV}$  would have jets recoiling against a highly boosted  $Z$  boson, the vertex where the electron originates in the tag and probe study is expected to have more tracks associated to it than a typical high-mass  $W \rightarrow e\nu$  process, where there may not be much else in the event.

A control region enriched in  $W$  boson production is defined for this purpose, and the full background estimate is compared to the observed events in this region. The control region is defined by inverting the separation requirement between the candidate photon and  $E_T^{\text{miss}}$ , and additionally requiring the photon transverse mass  $M_T = [2E_T^{\text{miss}} p_T^\gamma (1 - \cos \Delta\phi(E_T^{\text{miss}}, \gamma))]^{1/2}$  to be between 40 GeV and 150 GeV. To reduce the contribution from  $\gamma + \text{jets}$  events, photon  $p_T$  is capped at 400 GeV, above which  $\gamma + \text{jets}$  was observed to become the dominant source of events in this control region. All other selections are identical to the candidate event selection defined in Sec. 3. The upper bound on  $M_T$  together with the lower bound on  $p_T^\gamma$  and  $E_T^{\text{miss}}$  will in fact force the photon and  $E_T^{\text{miss}}$  to be closer than 1 radian in  $\phi$ , and thus the inversion of the photon- $E_T^{\text{miss}}$  separation is actually redundant.

Figure 9 shows the photon  $p_T$ ,  $E_T^{\text{miss}}$ , and  $M_T$  distributions from this control region. As it is visible from the plots, there are very few observed events because of the rather stringent requirement applied to obtain a pure  $W \rightarrow e\nu$  sample. Nevertheless, within the available statistical power, the comparison between the prediction and observation validates the electron misidentification background estimation method. For  $E_T^{\text{miss}} > 150 \text{ GeV}$ , 14 events are observed for a prediction of 11.2 events.

The final result of the measurement is

$$R_e = 0.0184 \pm 0.0040(\text{stat.}) \pm 0.0026(\text{fit model}) \quad (3)$$

which translates to the prediction of the electron misidentification background in the candidate events with  $E_T^{\text{miss}} > 170 \text{ GeV}$  of  $7.35 \pm 2.01(\text{syst.})$ , where the statistical uncertainty is from the size of the proxy sample, and the uncertainties on the  $R_e$  factor is all combined into the systematic uncertainty.

## 5.4 Hadron misidentification

Any analysis involving photons in final state is always subject to *fake*, photons from QCD multi-jet events. Specifically, these *fakes* occur when one of the high  $E_T$  jets fragments into an isolated  $\pi^0$  or  $\eta$  which is sufficiently collimated to appear as a single electromagnetic shower in the ECAL detector.

The fraction of hadronic activity from QCD which will pass the photon isolation selection requirements is small but the QCD production is large, so the overall production rate for *fake* photons coming from QCD is potentially large. This background is notoriously difficult to simulate using Monte Carlo (MC) techniques due to the cross section and fragmentation uncertainties as well as the large statistics requirement. We therefore use a data-driven approach. We select a sample of *fake* photons using a selection that is similar to that used for candidate

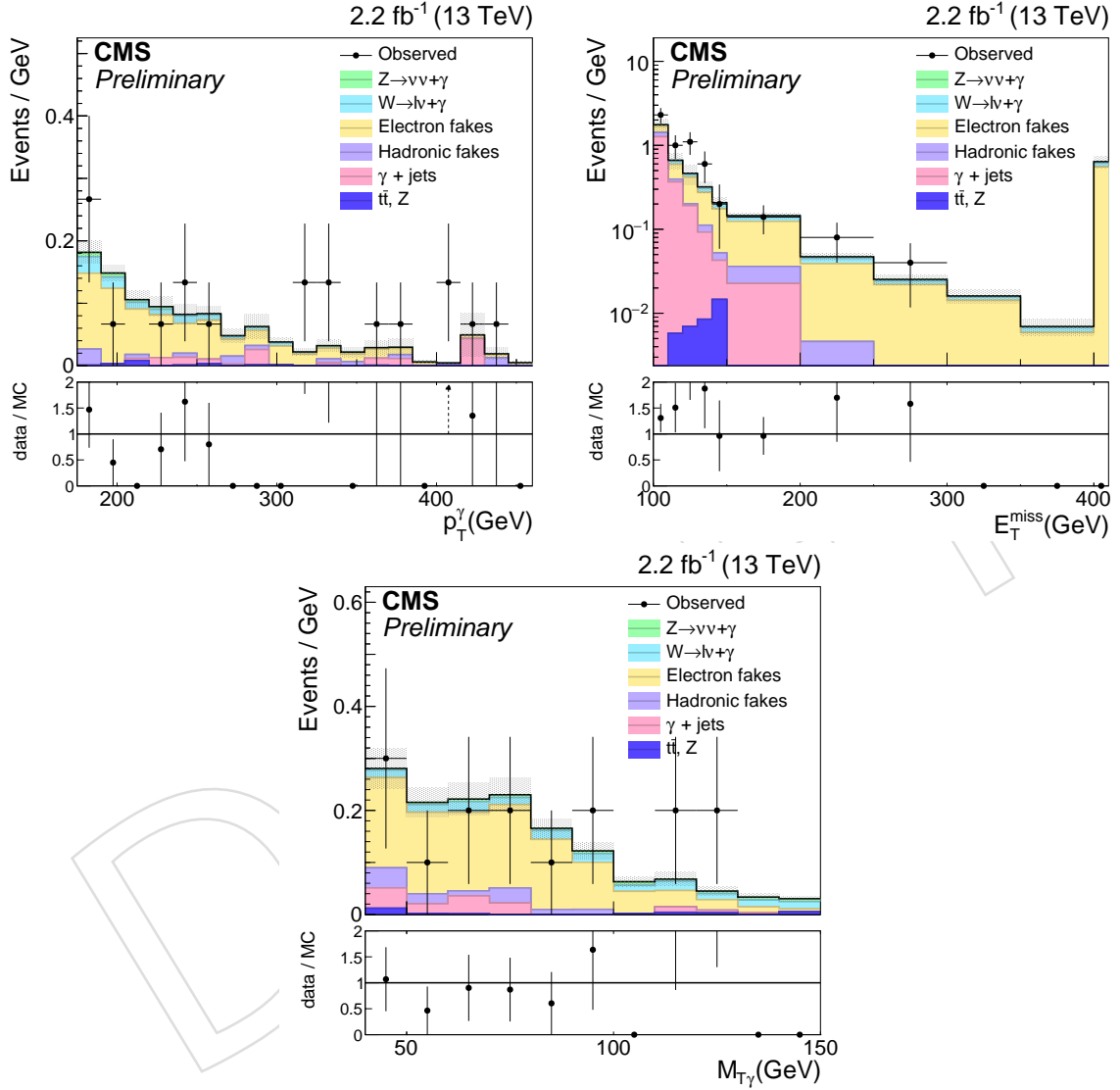


Figure 9: Photon  $p_T$  (top left),  $E_T^{\text{miss}}$  (top right), and  $M_T$  (bottom left) distributions in the  $W \rightarrow e\nu$  validation region overlaid with the total SM prediction. The photon  $p_T$  plot contains only events with  $E_T^{\text{miss}} > 140 \text{ GeV}$ . Similarly the  $E_T^{\text{miss}}$  plot contains events with  $175 < p_T^\gamma < 400 \text{ GeV}$ . The  $M_T$  plot is made applying both requirements.

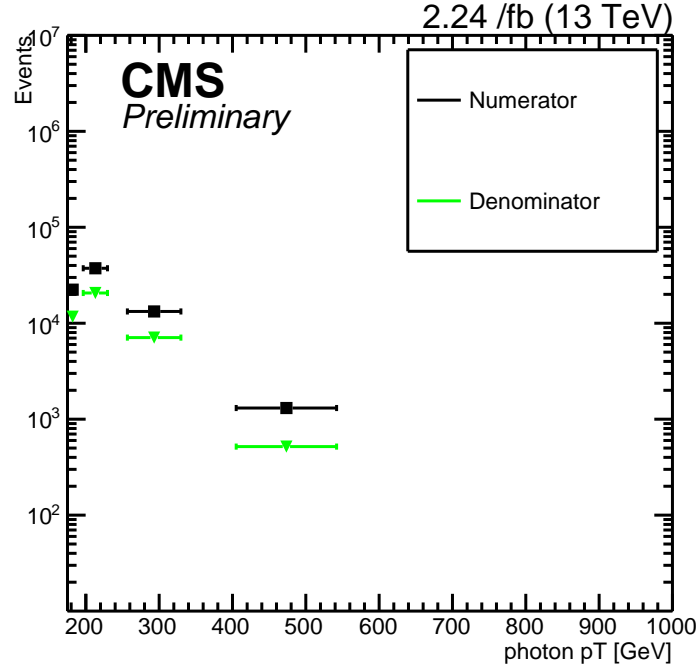


Figure 10: Raw number of events using the numerator (black) and denominator (green) selection criteria for the QCD *fake* ratio.

events and apply the fake ratio to provide a normalized estimate of the jet faking photon background. An advantage of such a data driven technique is that one does not need to know NLO  $k$ -factors or how to model effects like pileup or fragmentation.

For a realistic estimation of the fake ratio we use the shower shape properties of photons in the ECAL from data. We use a data control sample of  $E_T^{\text{miss}} < 30$  GeV which is well separated from the signal control region of  $E_T^{\text{miss}} > 140$  GeV. This sample is dominated by QCD multi-jet events. We define the fake ratio as the number of events with an object passing photon selection criteria used in candidate selection compared to the number of events containing a jet that can give rise to a *fake* photon object. The numerator in this ratio is the number of events that contain a photon which satisfies the the medium photon ID criteria, and the denominator is the number of events conatining a photon which fails the loose photon ID criteria, but passes a very loose selection. Both the numerator and denominator have in addition to the  $E_T^{\text{miss}} < 30$  requirement, selections to mitigate the effects of noncollision backgrounds and beam halo effects. Events in both the numerator and denominator are required also to have triggered at least one of the HLT trigger paths used in the event selection. The selections for the numerator and denominator are summarized in Tables 9 and 10 respectively. Figure 10 shows the raw number of events selected in the numerator and denominator as a function of  $p_T^\gamma$ .

The control sample where we measure the fake ratio has a considerable fraction of true isolated photons from inclusive QCD direct photon production processes. This contribution is estimated and the numerator of the raw fake ratio is scaled to reflect only the QCD component. We use the  $\sigma_{i\eta i\eta}$  templates from  $\gamma + \text{jet}$  Monte Carlo to determine the fraction of true photons using the fraction fitting facility in *ROOFIT*. The QCD templates are taken from data by choosing events within a side-band of charged isolation defined as  $(5) \text{ GeV} < \text{charged isolation} < (10) \text{ GeV}$ . This side band is chosen such that the signal contamination in the background template is small ( $< 2\%$ ).

Table 9: Requirements for events passing the numerator selections. In the QCD background sideband, the  $PFIso_{ch}$  requirement (\*) is changed to  $5 < \text{Max}(0.0, PFIso_{ch}) < 10$ . When selecting on MC, beam halo and seed timing requirements(\*\*) are omitted.

Numerator Selections			
photon ID	$\text{Max}(0.0, PFIso_n - \rho \cdot EA_n)$	$< 1.06 + 0.014p_T^\gamma + 0.000019(p_T^\gamma)^2$	
	$\text{Max}(0.0, PFIso_\gamma - \rho \cdot EA_\gamma)$	$< 0.28 + 0.0053p_T^\gamma$	
	$\text{Max}(0.0, PFIso_{ch})$	$< 1.37^*$	
	$(H/E)^\gamma$	$< 0.05$	
	hasPixelSeed	False	
QCD	$E_T^{\text{miss}}$	$< 30$	
noncoll	$\sigma_{i\eta i\eta}^\gamma$	$> 0.001$	
	$\sigma_{i\phi i\phi}^\gamma$	$> 0.001$	
	$MIP^{E_{tot}}$	$< 4.9 * *$	
	$ t_{\text{seed}}^\gamma $	$< 3 * *$	

Table 10: Requirements for events passing the denominator selections. Events must fail at least one of the loose photon ID requirements but pass a very loose photon ID selection. The bounds for the very loose selection are 5 times those for the loose selection.

Denominator Selections			
photon ID	Fail One	$\text{Max}(0.0, PFIso_n - \rho \cdot EA_n)$	$< 1.92 + 0.014p_T^\gamma + 0.000019(p_T^\gamma)^2$
		$\text{Max}(0.0, PFIso_\gamma - \rho \cdot EA_\gamma)$	$< 0.81 + 0.0053p_T^\gamma$
		$\text{Max}(0.0, PFIso_{ch})$	$< 3.32$
	Pass All	$\text{Max}(0.0, PFIso_n - \rho \cdot EA_n)$	$< \text{Min}(0.2p_T^\gamma, 5 \times [1.92 + 0.014p_T^\gamma + 0.000019(p_T^\gamma)^2])$
		$\text{Max}(0.0, PFIso_\gamma - \rho \cdot EA_\gamma)$	$< \text{Min}(0.2p_T^\gamma, 5 \times [0.81 + 0.0053p_T^\gamma])$
		$\text{Max}(0.0, PFIso_{ch})$	$< \text{Min}(0.2p_T^\gamma, 5 \times 3.32)$
		$(H/E)^\gamma$	$< 0.05$
QCD		hasPixelSeed	False
noncoll		$E_T^{\text{miss}}$	$< 30$
		$\sigma_{i\eta i\eta}^\gamma$	$> 0.001$
		$\sigma_{i\phi i\phi}^\gamma$	$> 0.001$
		$MIP^{E_{tot}}$	$< 4.9$
		$ t_{\text{seed}}^\gamma $	$< 3$

Figures 11 and 12 show the results of the template fitting in various  $p_T$  bins. The estimated fractions are calculated within  $\sigma_{i\eta i\eta} < 0.0102$  to match the photon candidate selection criteria used in the remainder of this analysis.

Figure 13 shows the final corrected fake ratio used in estimating the QCD background from data. The QCD estimate is made by selecting events which are identical in character to our candidate event sample but replacing the photon identification selection with the criteria from the denominator sample and applying the fake ratio as a function of  $p_T$ . This fake ratio is used to normalized a very small sample of events, which is representative of the small number of data QCD events which will share our candidate signal topology. The fake ratio is parametrized in the following form as a function of  $p_T^\gamma$ :

$$f_{p_T^\gamma} = 0.077 - 0.00004p_T^\gamma \quad (4)$$



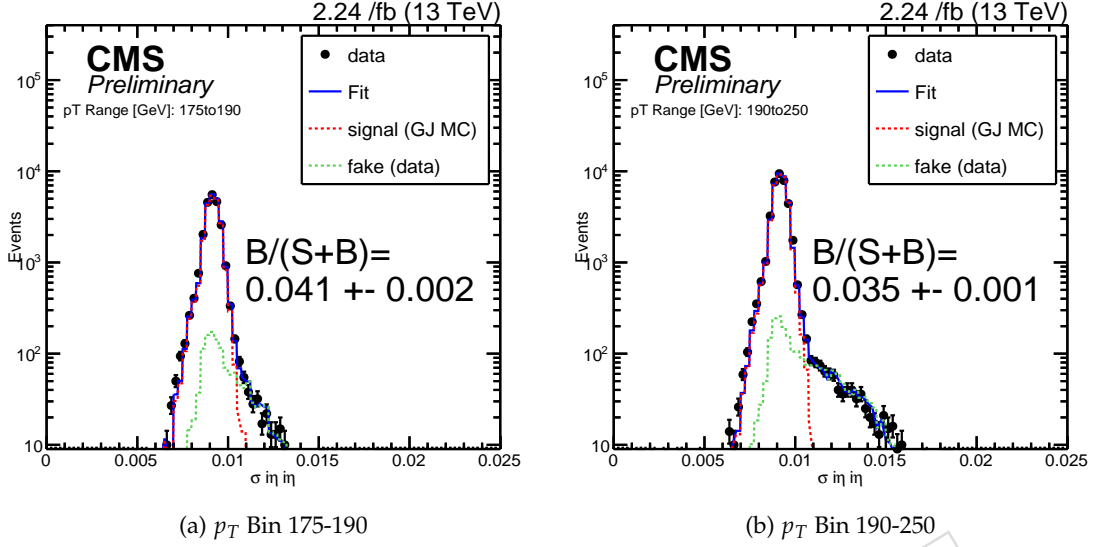


Figure 11: Template ( $\sigma_{i\eta i\eta}$ ) distributions and fits to QCD and true photon components in  $p_T$  bins 175-190 GeV and 195-250 GeV.

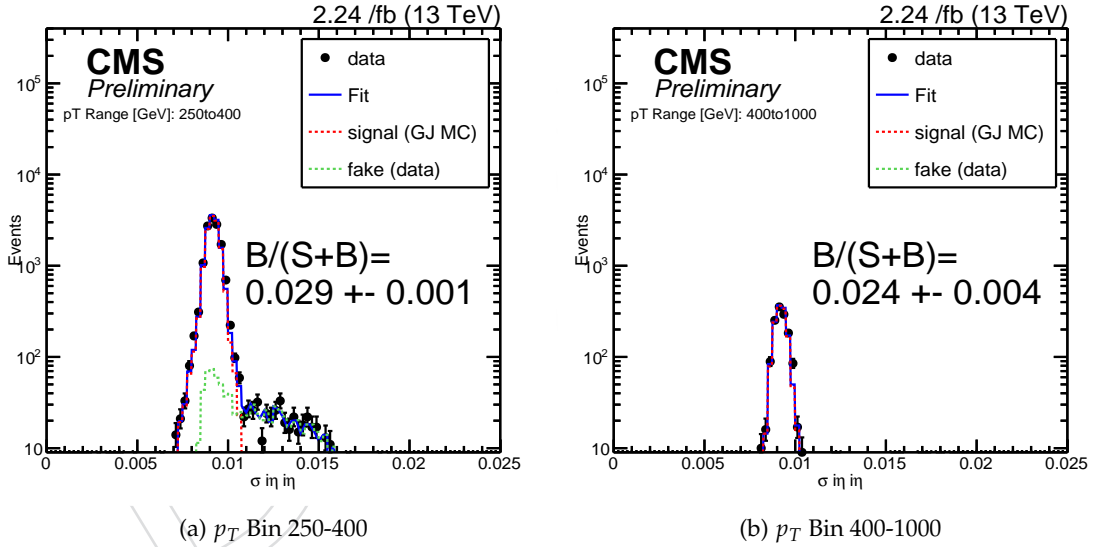


Figure 12: Template ( $\sigma_{i\eta i\eta}$ ) distributions and fits to QCD and true photon components in  $p_T$  bins 250-400 GeV and 400-1000 GeV.

The error on the estimated number is calculated by adding in quadrature the uncertainty arising from the following sources:

- The uncertainty due to different choices of sideband region. We choose two cases where the upper boundary of side is varied by 2 GeV on either side of the nominal threshold used
- Changing the definition of denominator by requiring only charged OR neutral isolation to fail.
- Varying the MET selection for control region to  $<15$  GeV and  $<40$  GeV.
- The bins size of shower shape templates. This is done by changing the bins size by

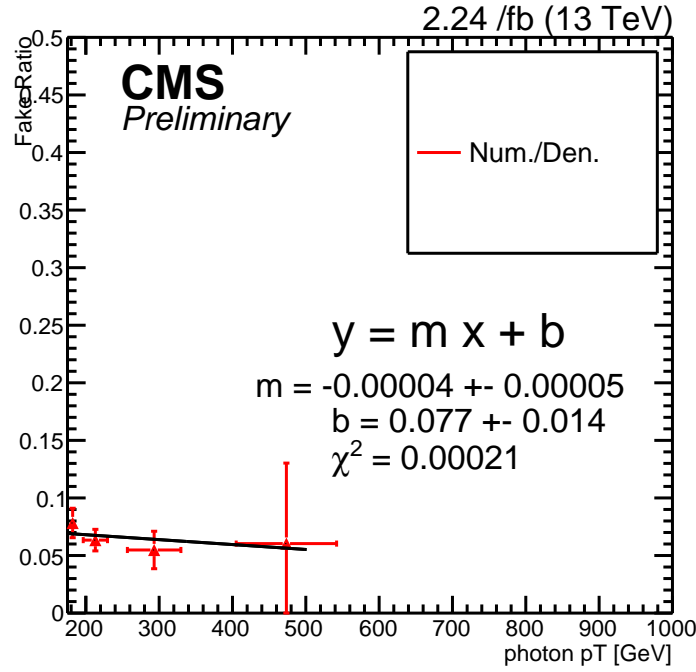


Figure 13: The corrected fake rate as a function of  $p_T$  for PF Medium photon identification selection.

0.5 and 2.0 times the nominal bin width.

- Fit uncertainty

The statistical uncertainty and side-band selection variation gives the maximum change in the fake ratio. Figure 14 summarizes the effect of these systematics on fake ratio. As a conservative approach, a total systematic uncertainty of 30% is used over the whole  $p_T$  range for fake ratio estimation and combined with statistical uncertainty.

The estimated total number of events for jet faking photon background from data is  $3.84 \pm 1.27$ .

## 5.5 $\gamma + \text{jets}$ background

### 5.5.1 Method 1

Because  $\gamma + \text{jets}$  background in the signal region arises from an extreme tail of a high-rate process, there is not enough MC simulation events to reliably predict the contribution. A data-driven method that exploits the dominance of the  $\gamma + \text{jets}$  process in the  $\min \Delta\phi(\text{jet}, E_T^{\text{miss}}) < 0.5$  region is devised in the following way.

First,  $E_T^{\text{miss}}$  distribution of single-photon events with  $\min \Delta\phi(\text{jet}, E_T^{\text{miss}}) < 0.5$  and  $> 0.5$  are plotted in the region  $E_T^{\text{miss}} < 120$  GeV. From a data-MC comparison study it can be shown that  $\gamma + \text{jets}$  is the dominant process in this low  $E_T^{\text{miss}}$  regime, regardless of  $\min \Delta\phi(\text{jet}, E_T^{\text{miss}})$  value. Figure 15 shows the two distributions compared to MC predictions. After subtracting the small contributions from other processes in respective  $\min \Delta\phi(\text{jet}, E_T^{\text{miss}})$  regions, the ratio of the two distributions are taken and then fit with a parametric function on the range  $E_T^{\text{miss}} \in [30, 120]$  GeV. This function is taken as the transfer factor that takes an observation in  $\min \Delta\phi(\text{jet}, E_T^{\text{miss}}) < 0.5$  to a prediction in  $\min \Delta\phi(\text{jet}, E_T^{\text{miss}}) > 0.5$ , given as a function of  $E_T^{\text{miss}}$ . This transfer function is then extrapolated to high  $E_T^{\text{miss}}$  region considering several functional

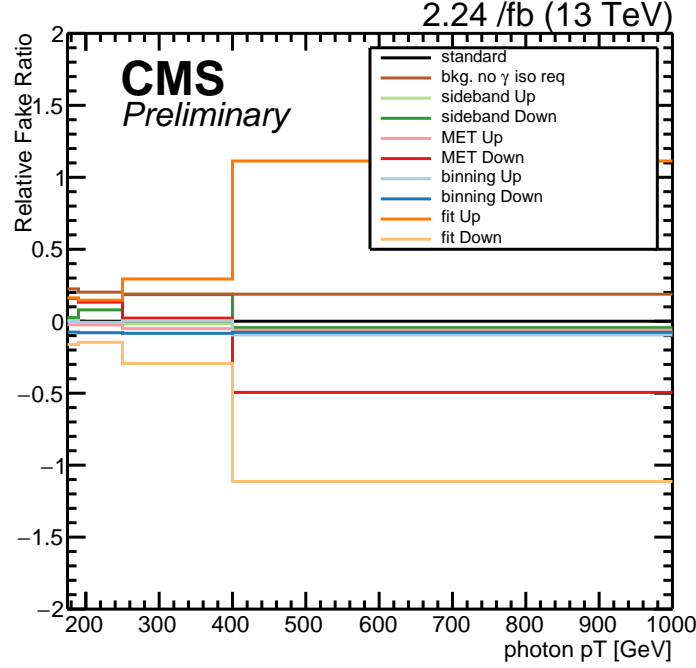


Figure 14: Change in fake ratio as a function of  $p_T^\gamma$  due to different sources.

forms (Fig. 16). We considered the following functions:

- a sum of exponentials  $\text{Expo}(x; C_1, \lambda_1, C_2, \lambda_2) = C_1 e^{\lambda_1 x} + C_2 e^{\lambda_2 x},$
- a gaussian with a tail  $\text{Gauss}(x; C, \sigma, a) = C \exp\left(\frac{-x^2}{(\sigma + ax)^2}\right).$

Finally, the distribution of events in the control region  $\min \Delta\phi(\text{jet}, E_T^{\text{miss}}) < 0.5$  with  $E_T^{\text{miss}} > 170 \text{ GeV}$  is multiplied by the extrapolated transfer factor, as shown in Figure 17. We take the prediction derived using the double exponential function as our nominal value and assign a 100% systematic uncertainty, resulting in a final prediction of  $0.006 \pm 0.006$   $\gamma$  + jets events in the signal region.

### 5.5.2 Method 2

As a cross check of the above method, we also investigated fitting the  $E_T^{\text{miss}}$  spectrums instead of their ratio. This adds some information as we can look at the full spectrum in the  $\min \Delta\phi(\text{jet}, E_T^{\text{miss}}) < 0.5$  region while we are limited to  $E_T^{\text{miss}} < 120 \text{ GeV}$  in the  $\min \Delta\phi(\text{jet}, E_T^{\text{miss}}) > 0.5$  region, and thus in the ratio as well.

After subtracting the small contributions from other processes in respective  $\min \Delta\phi(\text{jet}, E_T^{\text{miss}})$  regions, we fit the resulting  $E_T^{\text{miss}}$  distribution in each region with a parametric Rayleigh functions. The ratio of these functions is taken as the transfer factor that takes an observation in  $\min \Delta\phi(\text{jet}, E_T^{\text{miss}}) < 0.5$  to a prediction in  $\min \Delta\phi(\text{jet}, E_T^{\text{miss}}) > 0.5$ , given as a function of  $E_T^{\text{miss}}$ . The fits and the resulting resulting transfer factors are shown in Figure 18. We considered the

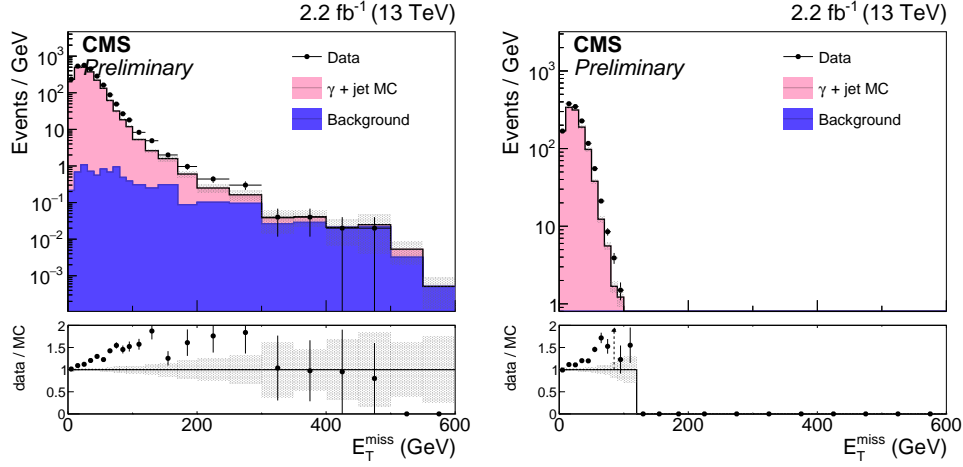


Figure 15:  $E_T^{\text{miss}}$  distributions of events with  $\min \Delta\phi(\text{jet}, E_T^{\text{miss}}) < 0.5$  (left) and  $> 0.5$  (right), up to  $E_T^{\text{miss}} = 120$  GeV.

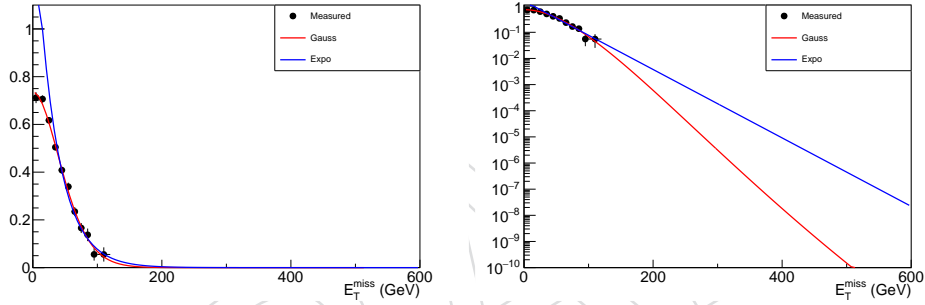


Figure 16: Analytic fits on the range  $E_T^{\text{miss}} \in [30, 120]$  GeV to the  $\min \Delta\phi(\text{jet}, E_T^{\text{miss}}) < 0.5$  to  $\min \Delta\phi(\text{jet}, E_T^{\text{miss}}) > 0.5$  transfer factor and their extrapolations to  $E_T^{\text{miss}} > 170$  GeV. See text for function definitions.

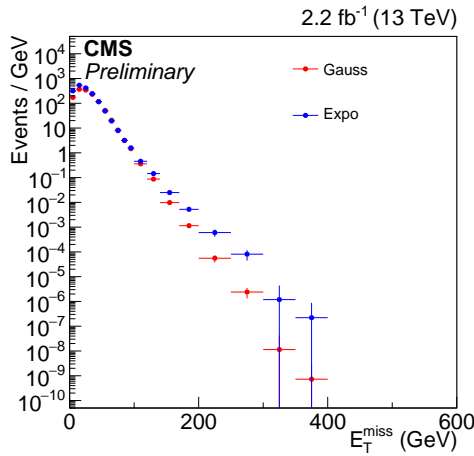


Figure 17: Predicted  $\gamma$ +jets yield as a function of  $E_T^{\text{miss}}$  derived from fitting the  $\min \Delta\phi(\text{jet}, E_T^{\text{miss}}) < 0.5$  to  $\min \Delta\phi(\text{jet}, E_T^{\text{miss}}) > 0.5$  transfer factor directly.

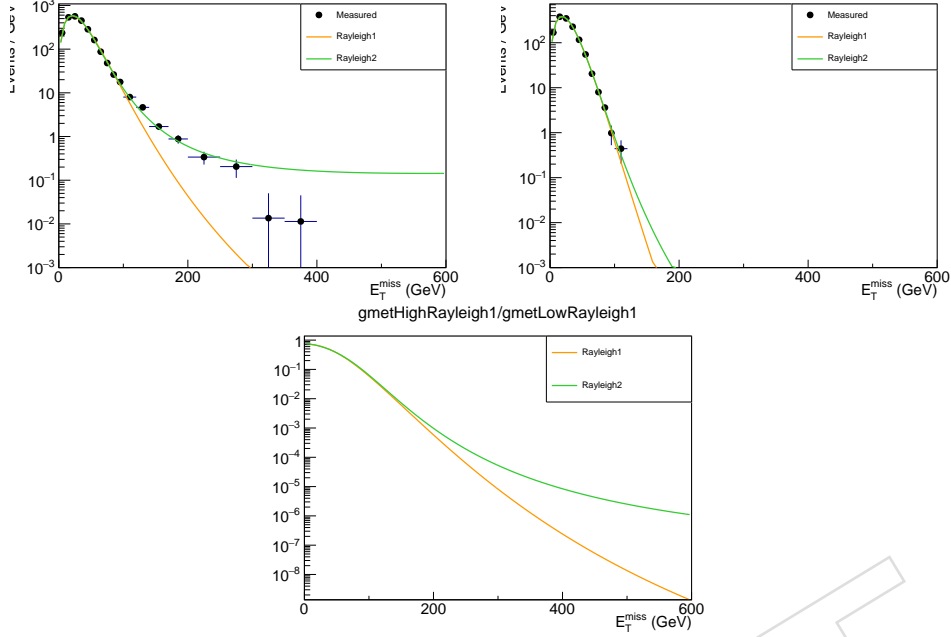


Figure 18: Analytic fits to the  $E_T^{\text{miss}}$  spectrum in the  $\min \Delta\phi(\text{jet}, E_T^{\text{miss}}) < 0.5$  (left) and  $\min \Delta\phi(\text{jet}, E_T^{\text{miss}}) > 0.5$  (right) regions and the resulting ratio (bottom) along with extrapolation. See text for function definitions.

following types of Rayleigh functions:

- one with two resolution parameters

$$\text{Rayleigh1}(x; C, \sigma, a) = C \exp \left( \frac{-x^2}{(\sigma + ax)^2} \right),$$

- one with three resolution parameters

$$\text{Rayleigh2}(x; C, a, b, c) = C \exp \left( \frac{-x^2}{a + bx + cx^2} \right).$$

Finally, the distribution of events in the control region  $\min \Delta\phi(\text{jet}, E_T^{\text{miss}}) < 0.5$  with  $E_T^{\text{miss}} > 170$  GeV is multiplied by the extrapolated transfer factor, as shown in Figure 19. We use the prediction using the Rayleigh function with three resolution parameters as our nominal value and assign a 100% systematic uncertainty, resulting in a final prediction of  $0.002 \pm 0.002$   $\gamma$  + jets events in the signal region, which is consistent with the estimate shown in Section 5.5.1.

### 5.5.3 Method 3

The third method of  $\gamma$  + jets background estimation is based on the assumption that the MC has a higher  $E_T^{\text{miss}}$  resolution, and therefore its  $E_T^{\text{miss}}$  spectrum must be smeared to predict the number of  $\gamma$  + jets events that may trickle down into the signal region. A proper way of smearing the  $E_T^{\text{miss}}$  would be to smear the momentum of the visible objects, in particular the jets, following known resolution uncertainties. We approach this problem in a short-cut way by comparing the data and MC  $E_T^{\text{miss}}$  distributions themselves, and convoluting the MC distribution with a smearing function.

To set up the measurement,  $\min \Delta\phi(\text{jet}, E_T^{\text{miss}}) < 0.5$  control sample is prepared in data and MC as in the previous two methods. The  $E_T^{\text{miss}}$  distributions of the  $\gamma$  + jets MC and the background samples are independently smoothed out by Guassian Kernel Estimation technique. The background distribution is completely fixed in terms of shape and the normalization, while the

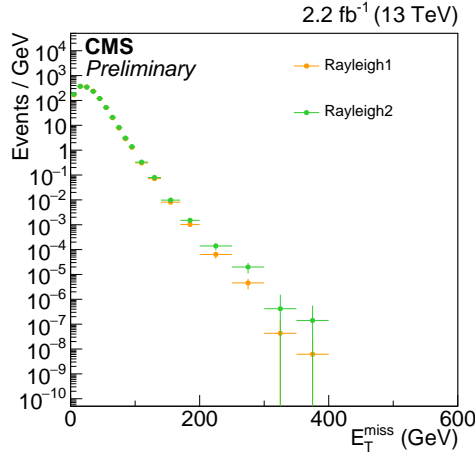


Figure 19: Predicted  $\gamma$ +jets yield as a function of  $E_T^{\text{miss}}$  derived from fitting the  $\min \Delta\phi(\text{jet}, E_T^{\text{miss}}) < 0.5$  (left) and  $\min \Delta\phi(\text{jet}, E_T^{\text{miss}}) > 0.5$  (right) regions and taking the resulting ratio as the transfer factor.

$\gamma$  + jets distribution is convoluted with a Landau function with its mean and width floating. The sum of the backgrounds and  $\gamma$  + jets distributions is then made into a composite PDF which is fit to the data  $E_T^{\text{miss}}$  distribution via binned likelihood maximization. Figure 20 shows the data  $E_T^{\text{miss}}$  distribution,  $\gamma$  + jets distribution without smearing,  $\gamma$  + jets distribution smeared with best-fit parameters, and the full fit result.

The end products of this method are the mean and width of the Landau function, which are -0.731 GeV and 0.510 GeV, respectively. This smearing function is then used to alter the  $E_T^{\text{miss}}$  value of the  $\gamma$  + jets MC sample in the  $\min \Delta\phi(\text{jet}, E_T^{\text{miss}}) > 0.5$  signal region. This smearing approach has another benefit, which is that the same MC event can be resampled multiple times to approximate the  $E_T^{\text{miss}}$  distribution that would be obtained from a larger sample.

However, even with 10 resampling from each  $\gamma$  + jets event, the predicted contribution of  $\gamma$  + jets in the signal region is 0. On the other hand, 10 resampling brings the effective sample sizes sufficiently large that all events in all  $H_T$  bins have event weight of  $\mathcal{O}(10^{-1})$ . Therefore the prediction is not statistically limited any more.

## 5.6 Non-collision background

### 5.6.1 Composition

Non-collision background arise from multiple sources, with the only commonality being that they appear as an isolated high-pT photon, often with very little activity in the event because coincidence with hard scatterings is rare, and consequently a large  $E_T^{\text{miss}}$  pointing away from the photon candidate. The known sources are:

- Beam halo

Bremsstrahlung by the beam halo muon around the ECAL volume will generate an actual physical EM shower in the ECAL crystals. Large energy deposit is expected to be rare, but it is indicated that there the rate of beam halo penetration during the 2015 run was substantial. Characteristic feature of the shower caused by the halo particles include coincident hits in the barrel muon system and a “trail” of low-energy clusters in ECAL along the particle trajectory. The CSC beam halo filter described in Sec. ?? exploits the former, while the MIP total energy variable of the photon object captures



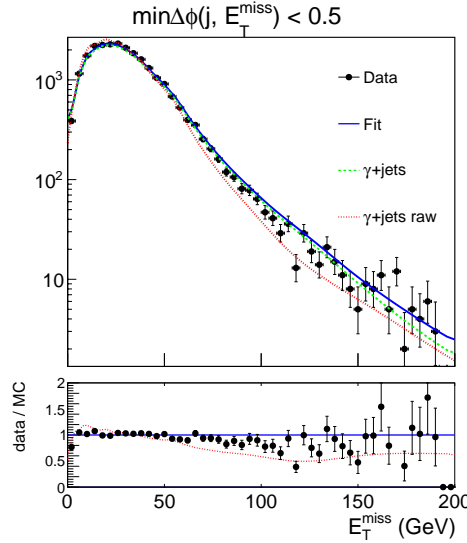


Figure 20:  $E_T^{\text{miss}}$  distributions in  $\min \Delta\phi(\text{jet}, E_T^{\text{miss}}) < 0.5$  control samples. The sum of  $\gamma + \text{jets}$  and backgrounds (blue curve) is fit to data (black dots). Red dotted curve is the  $\gamma + \text{jets}$  without any smearing procedure.

the latter.

- Spikes

Since 2010 it is known that the ECAL barrel avalanche photodiode (APD) can sporadically undergo a large discharge that correspond to up to several TeV of energy deposit. Unless the spike coincides with pileup or other form of genuine energy deposit in the crystal around the spiking APD, the resulting cluster will consist of a single crystal. Therefore the variable  $s_4$ , defined as the ratio of the rec hit energy of the seed crystal over the energy sum of the neighboring 4 crystals, can be used to efficiently reject such spurious clusters. Typically  $s_4$  is required to be less than 0.95.

- Local noise

Noise in the ECAL photodiodes or the electronics can also result in spurious clusters. Such clusters have similar characteristics as the spike signal, but are geographically localised to specific crystals. ECAL detector performance group (DPG) is regularly searching for noisy channels, and if found masking them from reconstruction. However there are fringe cases where the noise rate is quite not enough to be detected by the DPG but is sufficient to appear in the analysis candidate samples.

The most significant local noise sources are eliminated by requiring  $s_4 < 0.95$  on the candidate photons. For the remaining two sources, it was observed in Run 1 that the clusters caused by beam halo and spikes have distinctive distributions of the seed crystal timing. Therefore, the first step in estimating the contribution of the non-collision background is to look at the full timing distribution of the candidate photons. Because the default supercluster reconstruction algorithm discards ECAL hits with  $|t| > 3 \text{ ns}$ , a full re-reconstruction of the 2015 data is performed removing this constraint.

Figure 21 shows the timing distribution of barrel photon objects with  $p_T > 170 \text{ GeV}$  and  $\sigma_{\text{ini}} < 0.0102$  in events with  $E_T^{\text{miss}} > 170 \text{ GeV}$ . This distribution, which obviously consists of at least two distinct populations, is fit with three templates: halo, and spikes, and prompt. The halo template is formed by photons with MIP total energy  $> 4.9 \text{ GeV}$ . As a cross check, this template is compared to what is obtained by requiring the CSC beam halo tagger to have

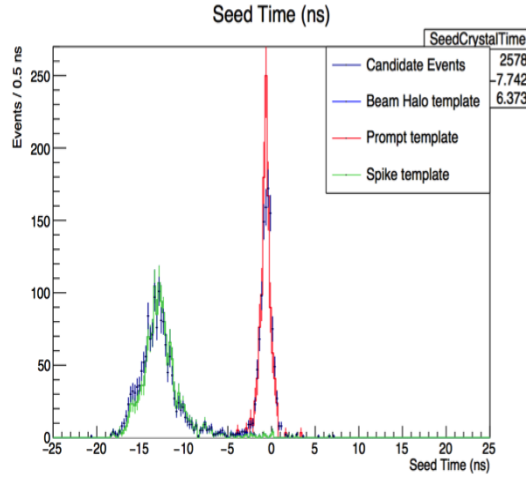


Figure 21: Timing distribution of candidate-like photons in events with  $E_T^{\text{miss}} > 150 \text{ GeV}$  obtained by full re-reconstruction of 2015 data. The three templates used in the fit are in Fig. 34.

fired, and is confirmed to be consistent. The spike template comes from photons where one of the shower shape variables ( $\sigma_{i\eta i\eta}$  or  $\sigma_{i\phi i\phi}$ ) have nonphysically small values, i.e.,  $< 0.001$ . The prompt template, which represents the timing distribution of EM objects emerging from the pp collisions, is made using the candidate sample in which the photon candidates are required to have a pixel seed match. Such sample is dominated by  $W \rightarrow e\nu$  events. This template is also cross-checked against a jet-like template, where the photon object is required to be nonisolated and pass only a loose shower shape requirement. The three templates and their cross checks are shown in Fig. 34.

From studying these distributions, it is concluded that the leakage of the spike population into the signal region is negligible, and thus what remains to be estimated is the beam halo background.

### 5.6.2 Beam halo estimate using the timing templates

Because the photons in re-reconstructed data cannot be matched one-to-one to those in the candidate sample, the timing fit is repeated on the latter with only the halo and prompt templates. The template sample definitions are the same as above. The fit target distribution is formed from photons passing the full selection except for the timing and shower shape requirements. The fit yields an estimate of  $2.54 \pm 3.07$  beam halo events in the signal region as shown in Figure 23.

However, it was later noted that there is a correlation between the width in  $\eta$  direction and the seed time of the showers caused by halo. Figure 24 shows the time distribution of halo candidate showers, using the same definition as above, in three different slices of  $\sigma_{i\eta i\eta}$ . The effect is understood to originate from the geometry of ECAL crystals. While the electromagnetic shower from the MIP bremsstrahlung develops along the  $z$  direction of the detector regardless of the shower location, the ECAL crystals have varying tilt angles to realize a projective geometry. This results in the ECAL “seeing” the halo showers to be narrower in  $\eta$  direction for high  $|\eta|$  regions, where the crystals are more aligned with the shower development. In addition, for MIPs that arrive synchronously to the proton bunches, shower in high  $|\eta|$  appears more like a prompt shower caused by a particle originating from the interaction point, giving a time profile that peaks closer to 0. The net result is a discrepancy in timing profiles between an

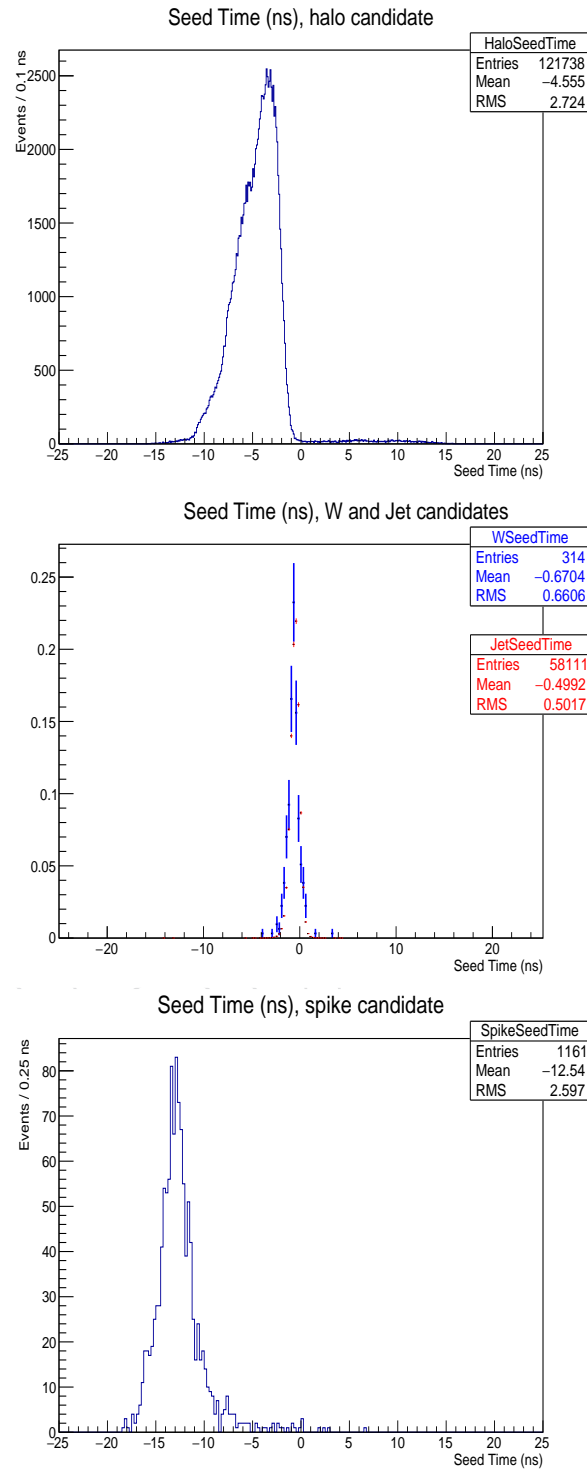


Figure 22: Timing distribution templates for halo, prompt, and spike candidates.

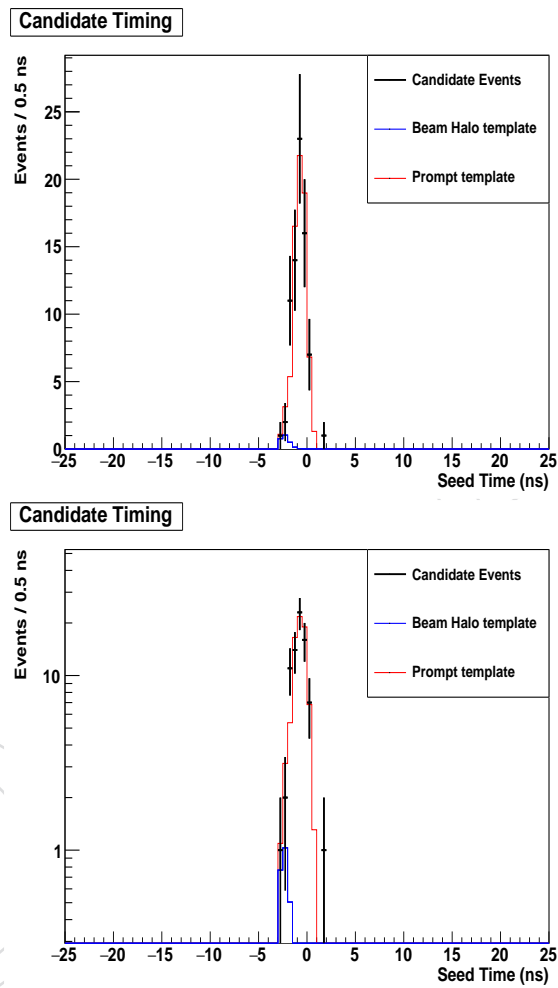


Figure 23: Timing fit to estimate the beam halo contamination in the signal region, in linear and log scales.

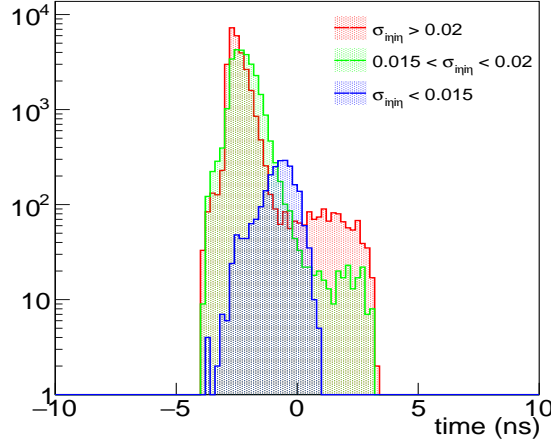


Figure 24: Seed crystal time of halo candidates in three different  $\sigma_{i\eta\eta}$  slices.

inclusive halo candidate sample, which is dominated by low- $|\eta|$ , wide showers, and a sample that more closely resembles the actual beam halo background in the analysis signal region. On the other hand, requiring  $\sigma_{i\eta\eta} < 0.0102$  as for the candidate photons will reject almost all of the halo candidates, making it impossible to estimate the halo background reasonably using this control sample. Therefore, the timing template fit above is repeated with a shower shape requirement of  $\sigma_{i\eta\eta} < 0.015$  on the halo template as a compromise. The fit (Fig. 25) yields an estimate of  $5.9 \pm 4.7$  beam halo events in the signal region.

To translate this inclusive result into differential (distribution) predictions, the halo control sample defined by MIP total energy  $> 4.9$  GeV is used to model the various distributions of the halo showers, and is weighted to normalize the total contribution to 5.9 events.

### 5.6.3 Beam halo estimate from the tagger efficiency estimates

Given an additional tagging criteria, the number of halo within the prompt window can be estimated using an additional method. Assuming that the efficiency of the two tagging algorithms are uncorrelated, then the following relations can be specified:

$$N_H^{T1} = \epsilon_{T1} \times N_H \quad (5)$$

$$N_H^{T2} = \epsilon_{T2} \times N_H \quad (6)$$

$$N_H^{T1T2} = \epsilon_{T1} \times \epsilon_{T2} \times N_H \quad (7)$$

where  $N_H^{T1}$ ,  $N_H^{T2}$  are the number of events which are tagged by the first and second tagger respectively,  $N_H^{T1T2}$  is the number of halo events which is tagged by both taggers,  $\epsilon_{T1}$  and  $\epsilon_{T2}$  are the efficiencies of the first and second taggers respectively and  $N_H$  is the total number of halo events. One can thus solve for the efficiency of each of the taggers, and also calculate the total remaining halo events. In data without sigmaietaieta cut, we observe 8153 events tagged by the CSCFlag, and 6571 events tagged by the MIP tagger. Of those events 2600 events are tagged by both. So using the first and third equations, we have  $\text{Eff}(\text{Csc}) = 0.39$  and using second and third equation,  $\text{Eff}(\text{MIP}) = 0.31$ . And then last equation yields  $N_{\text{halo}}$  estimate to be  $20605 \pm 296$ , where uncertainty is statistical.

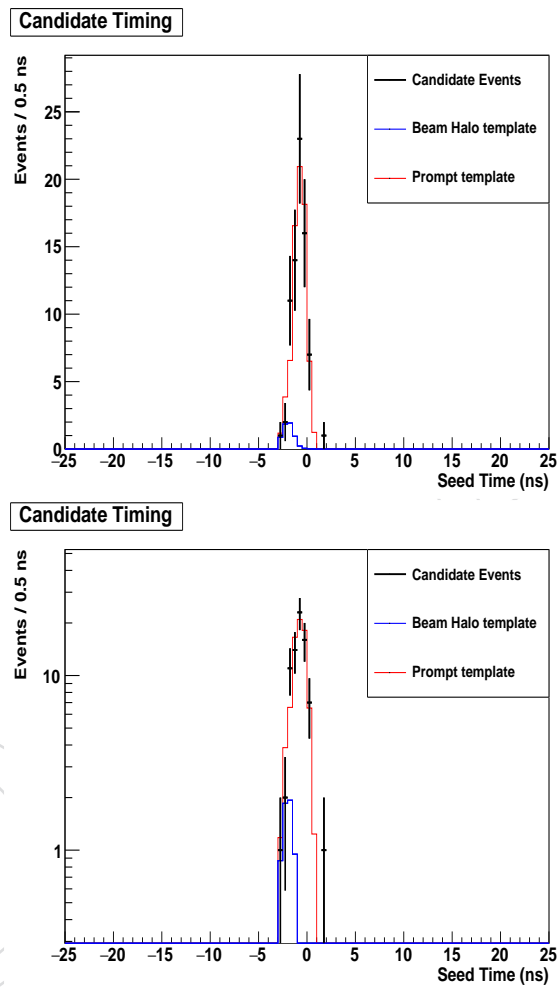


Figure 25: Timing fit to estimate the beam halo contamination in the signal region, in linear and log scales.



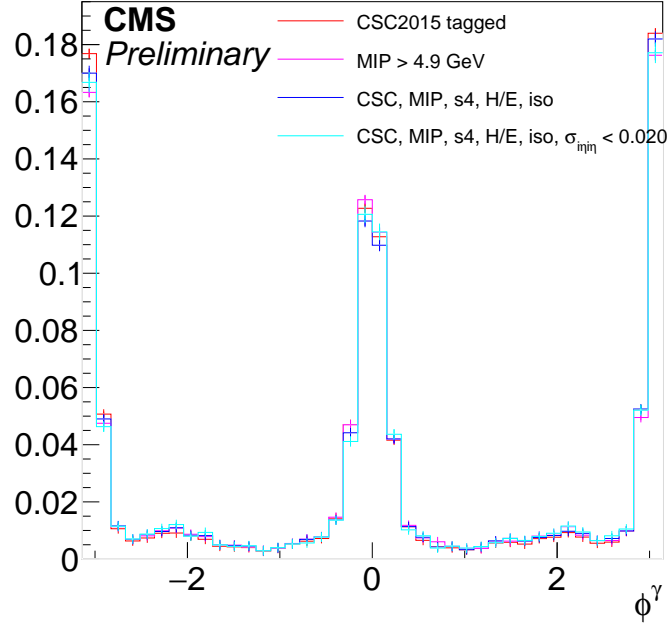


Figure 26:  $\phi$  distribution of the halo-like showers, tagged in multiple ways. Histograms are normalized to unity. The cyan histogram is the  $\phi$  distribution after applying photon identification selections except for the shower shape. It can be seen that the  $\phi$  distribution is highly stable against the listed identification selections.

We repeat the study after applying the sigmaieta cut (0.01), and observe 0 events tagged by the CSCFlag, and 7 events tagged by the MIP tagger. Of those events 0 events are tagged by both. We assume efficiencies are independent of shower shape and dominated by the statistical uncertainty on the number passing both the cuts, which yields beam halo estimate of  $9.12^{+4.17}_{-2.86}$  from MIP tagger.

This estimate is in agreement with the estimate which we obtained by fitting in the prompt region.

#### 5.6.4 Beam halo estimate using the azimuthal angle distribution

Because the beam halo particles are produced through complex LHC machine effects, it is natural that the observed location of the halo showers is not symmetric in the azimuthal angle in the detector coordinates. Figure 26 is a  $\phi$  distribution of the halo showers obtained from the single photon data set, requiring  $E_T^{\text{miss}} > 140$  GeV. Here, halo showers are defined as those that fail the MIP-tagging and in the event tagged by the CSC beam halo tagger. On the other hand, aside from local effects such as noisy crystals (see Sec. 5.6.1), reconstructed shower from all other sources should be symmetric in  $\phi$ . Therefore, a two-template fit to the  $\phi$  distribution of the photons in the candidate sample, where the templates are that of the halo shower and a uniform distribution, will reveal the amount of beam halo background present in the sample.

For the distribution of Fig. 26 to be a valid template for halo showers, it must be first confirmed that its shape is invariant under photon selection requirements. However, further study of the  $\phi$  distribution of the halo showers indicates that the relative strength of the two prominent peaks in the distribution may change under the  $\sigma_{\text{in}\eta}$  selection requirement. To explain this phenomenon, one needs to look at the  $\eta$  distribution of the shower populations near  $\phi \sim 0$

and  $\phi \sim \pi$ , which is shown in Fig. 27 top. Meanwhile, halo showers tend to have narrower shape in  $\eta$  direction when occurring at high  $\eta$ , due to the projective geometry of the ECAL crystals (Fig. 27 bottom). Combining the two observations, the conclusion is that the stringent requirement on the narrowness of the shower in the photon selection will preferentially reduce the  $\phi \sim 0$  population.

It is nevertheless possible to perform the aforementioned two-template fit by folding the  $\phi$  distribution such that the two peaks of the halo showers coincide. The fit model has the fraction of the halo component  $h$  as the only floating parameter. The halo template histogram shown in Fig. 28 is directly used as the probability distribution function of the halo, without smoothing or parametrizing its shape. To match the positions of the peaks in the halo template, a slightly shifted angle  $\phi' = \phi + 0.005$  is used. Figure 28 shows the folded  $\phi$  distribution of the candidate sample and an arbitrarily normalized halo template, together with the result of the unbinned maximum-likelihood fit.

Since the nominal fit predicts a halo background of less than 0.01 events, we set a 95% confidence upper limit on the possible background contribution, based on a  $\text{CL}_{s+b}$  value where the uniform distribution is treated as the background and the halo contribution as the signal. Possible  $h$  hypothesis are scanned to find a value  $h^{95}$ , above which the probability of making an observation less compatible with the hypothesis than the actual data is less than 5%. For the test statistic, the negative log likelihood ratio

$$q_h = -2 \ln \frac{\mathcal{L}_h}{\mathcal{L}_{\hat{h}}}$$

is used, where  $\hat{h} < h$  is the best-fit fraction bounded by  $h$ , and  $\mathcal{L}_h$  is the unbinned likelihood of data under the hypothesis  $h$ . For each test  $h$ , 10000 toy data sets each with the same number of events as the candidate sample are generated. For each toy data set,  $q_h$  is computed and is compared to that computed on the observed candidate sample under the hypothesis  $h$  ( $q_h^{\text{obs}}$ ). The fraction of data sets with  $q_h > q_h^{\text{obs}}$  is the  $\text{CL}_{s+b}$  value.

With a scan step size of 0.001,

$$h^{95} = 0.057$$

is obtained. For 77 observed events as detailed in Sec. 8, this translates to a predicted upper limit of 4.4 beam halo events in the signal region.

## 5.7 $\tau \rightarrow \gamma$ misidentification

We investigate the  $\tau \rightarrow \gamma$  fake rate by seeing how the photon ID selection affects reconstructed photons matched to generator taus in the  $W \rightarrow \ell \nu$  MC simulation sample. Table 11 shows the raw MC event yields and efficiencies after applying each step of the photon ID for events passing our event selection. Table 12 shows the same but having removed the tau veto as well as the  $E_T^{\text{miss}}$  and  $\min \Delta\phi(\text{jet}, E_T^{\text{miss}})$  cuts from the selection. As the efficiencies are roughly the same up until there are no events left in the full signal selection, we take the final efficiency from Table 12, as the rate at which taus fake photons in our signal region. Because the  $W \rightarrow \ell \nu$  sample was divided into different generator-level  $H_T$  bins, we split the 119 events in the third row of Tab. 11 into yields from individual  $H_T$  bins, scale them to the integrated luminosity, multiply the results by the efficiency of a high-pT photon-like tau to pass the full selection estimated from Tab. 12 (4/1449), and add them back together. This results in a prediction of  $0.02 \pm 0.02$  events due to tau fakes in the signal region. The uncertainty is fully statistical.

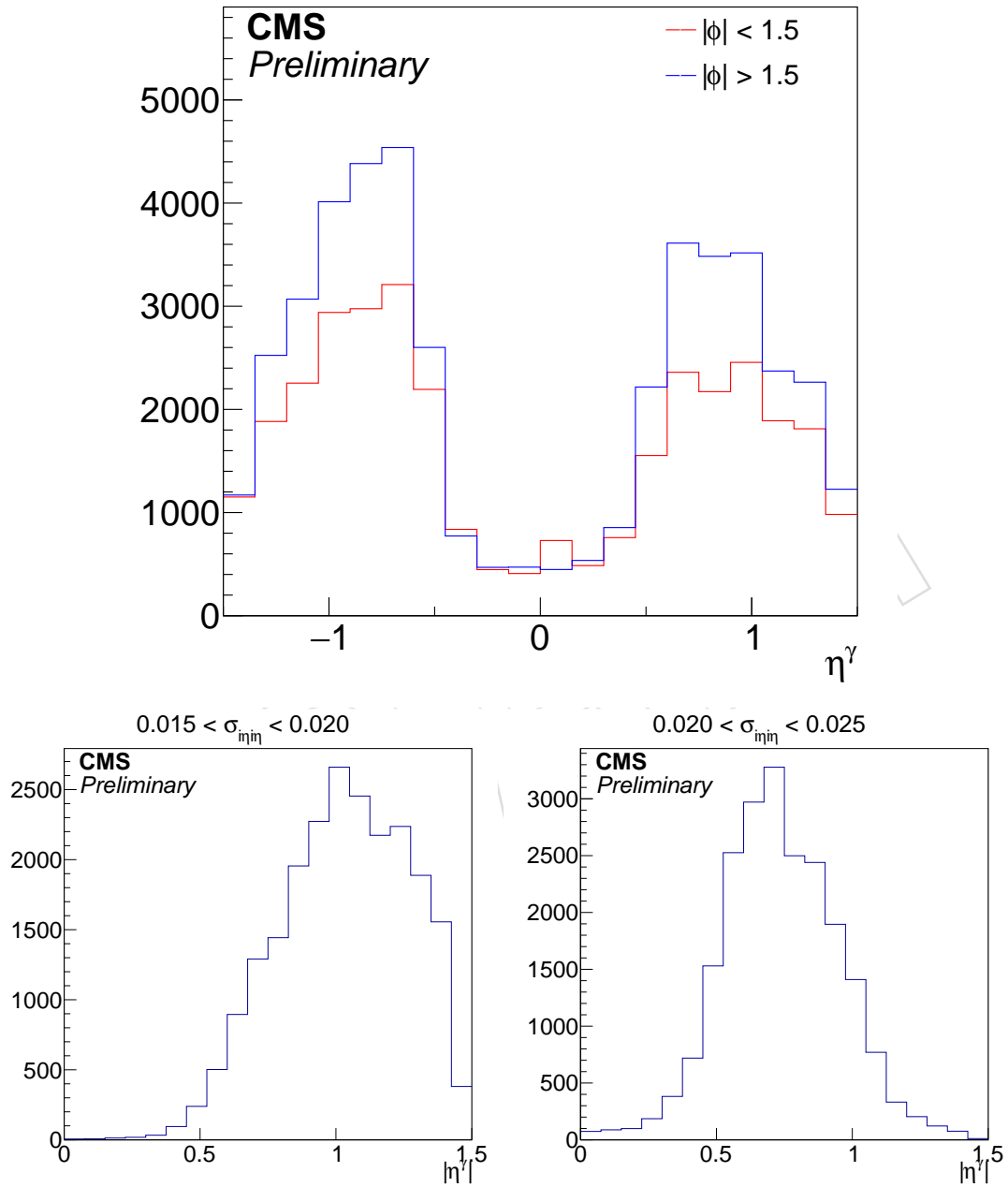


Figure 27: Top:  $\eta$  distribution of the halo-like showers with  $|\phi| < \pi/2$  and  $|\phi| > \pi/2$ . Bottom: shift in the  $\eta$  distribution of the halo-like showers with respect to the requirement on  $\sigma_{i\eta i\eta}$ .

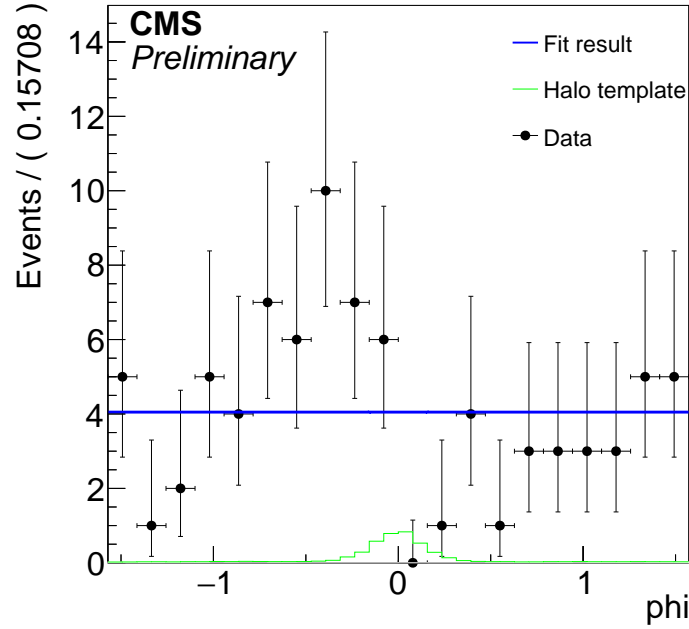


Figure 28: Folded  $\phi + 0.005$  distribution of the candidate sample and the halo template. The halo template is normalized to  $h = 0.057$  (see below). When the two-component model is fit to the data, the best fit result predicts absolutely 0 halo contribution.

Cut	Raw MC yield	Efficiency (%)
tau matched	2298	100.0000
isEB	1363	59.3124
pT > 175	119	5.1784
pass hOverE	39	1.6971
pass nhIso	22	0.9574
pass chIso	2	0.0870
pass phIso	0	0.0000
pass sieie <	0	0.0000
pass eveto	0	0.0000
pass sieie >	0	0.0000
pass s4	0	0.0000
pass mip energy	0	0.0000
pass time	0	0.0000

Table 11: Raw  $W \rightarrow \ell \nu$  MC event yields for reconstructed photons matched to generator level taus with full signal-like selection.

Cut	Raw MC yield	Efficiency (%)
matched to tau	76593	100.0000
isEB	37466	48.9157
pT > 175	1449	1.8918
pass hOverE	472	0.6162
pass nhIso	288	0.3760
pass chIso	51	0.0666
pass phIso	37	0.0483
pass sieie <	14	0.0183
pass eveto	4	0.0052
pass sieie >	4	0.0052
pass s4	4	0.0052
pass mip energy	4	0.0052
pass time	4	0.0052

Table 12: Raw  $W \rightarrow \ell \nu$  MC event yields for reconstructed photons matched to generator level taus with tau veto,  $E_T^{\text{miss}}$  cut, and  $\min \Delta\phi(\text{jet}, E_T^{\text{miss}})$  cut relaxed.

## 6 Validation using muon control regions

### 6.1 $Z(\nu\nu)\gamma$ data driven estimate

To cross-check the  $Z(\nu\bar{\nu}) + \gamma$  background estimate from the MC sample, we performed an estimation of its contribution to the total background using data. As the  $Z(l\bar{l})$  and the  $Z(\nu\bar{\nu})$  events share similar kinematic characteristics, the  $Z(\nu\bar{\nu})$  decay can be simulated by reinterpreting the lepton pair coming from the Z boson leptonic decay as missing energy. This study is largely inspired from [? ].

The sample of  $Z(l\bar{l})$  events is selected by requiring two leptons of the same flavor (muons or electrons) with opposite-sign charges each with  $p_T > 10$  GeV and an invariant dilepton mass between 60 and 120 GeV. The isolation and ID requirements on these leptons is the same as is used for the lepton veto in the signal selection. The hadronic recoil is used in place of  $E_T^{\text{miss}}$  in the signal selection, where the former is defined by the vectorial sum of  $\vec{p}_T^{\text{miss}}$  and the lepton transverse momenta. Lepton veto and angular restriction between jet and  $E_T^{\text{miss}}$  are dropped from the selection criteria.

The number of  $Z(\nu\bar{\nu})$  events can then be predicted using:

$$N(Z \rightarrow \nu\bar{\nu}) = \frac{N_{\text{obs}} - N_{\text{bgd}}}{A \times \epsilon} R \left( \frac{Z \rightarrow \nu\bar{\nu}}{Z \rightarrow l\bar{l}} \right) \quad (8)$$

where  $N_{\text{obs}}$  is the number of observed di-muon events,  $N_{\text{bgd}}$  is the number of background events contributing to the di-muon sample,  $A$  is the fiducial and kinematic acceptance of the detector and the efficiency of the Z-mass window cut, and  $R$  is the ratio of the branching fractions for the Z decay to neutrino and a pair of muons or electrons. The event selection efficiency,  $\epsilon$ , is defined as the efficiency of reconstructing leptons passing all the identification and isolation criteria and with an invariant criteria between 60 and 120 GeV, given that they are within the detector acceptance. The quantity  $A \times \epsilon$  is taken from MC as the ratio of reconstructed events passing the event selection to those passing at the generator (MC truth) level.

In this study, the parameters of Eq.8 take the following values:

- The number of events observed in data is:

$$N_{obs} = 14.0 \pm 3.7 \quad (9)$$

- $N_{bgd}$  is taken as the difference between  $N_{obs}$  and the number of simulated  $Z\gamma \rightarrow \nu\nu\gamma$  events in this phase space giving

$$N_{obs} - N_{bgd} = 11.9 \pm 3.4 \quad (10)$$

- $A \times \epsilon$  is defined as the fraction of all generated events where the leptons pass the dilepton pair selection, using MC generator level information:

$$A \times \epsilon = (59.2 \pm 0.6)\% \quad (11)$$

- $R$  is obtained from [?] for  $l = e, \mu$ :

$$R \left( \frac{Z \rightarrow \nu\bar{\nu}}{Z \rightarrow l\bar{l}} \right) = 2.971 \pm 0.001 \quad (12)$$

Putting this together then, the total number of expected events coming from the process  $Z\gamma \rightarrow \nu\bar{\nu}\gamma$  using this data-driven technique is  $59.7 \pm 17.3$  events. This is in agreement with the value predicted using simulation within statistical uncertainty. Figure 29 shows the comparison between data and simulation in the invariant mass of the dilepton pair.

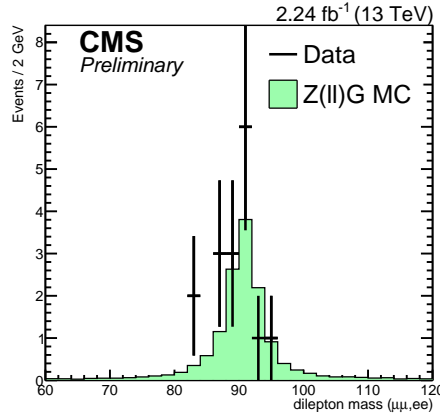


Figure 29: The invariant mass of the dilepton object required in this selection.

## 6.2 Single muon control region

To validate the  $W + \gamma$  MC simulation, observed events are compared to MC estimates in the single-muon control region. This control region is defined by the following requirements:

- At least one photon candidate with  $p_T > 140$  GeV
- Exactly one good muon candidate with  $p_T > 30$  GeV
- No other muons passing a looser selection
- $U = |\vec{E}_T^{\text{miss}} + \vec{p}_T^\mu| > 100$  GeV
- Separation of  $E_T^{\text{miss}}$  and the photon candidate in the azimuthal angle by more than 2 radians
- No electron, or tau

- No jet within 0.5 radians in the azimuthal angle from the  $E_T^{\text{miss}}$  direction
- Pass anomalous event filters (“MET filters”)

Collision events are taken from the SingleMuon dataset, with the muon candidate matched to the HLT object. The photon  $p_T$  threshold is motivated by the generator-level threshold of 130 GeV imposed on the  $W + \gamma$  MC sample. The variable  $U$  is used instead of  $E_T^{\text{miss}}$  to select events in order to make this control region similar to the  $W + \gamma$  events in the signal region, where the lepton can be out of the detector acceptance and therefore is accounted as missing momentum.

Figure 30 is the comparison of the distributions in  $p_T^\gamma$ ,  $E_T^{\text{miss}}$ , and  $U$ .  $W + \gamma$  production is predicted to dominate in this control region, and a good agreement between data and prediction is observed.

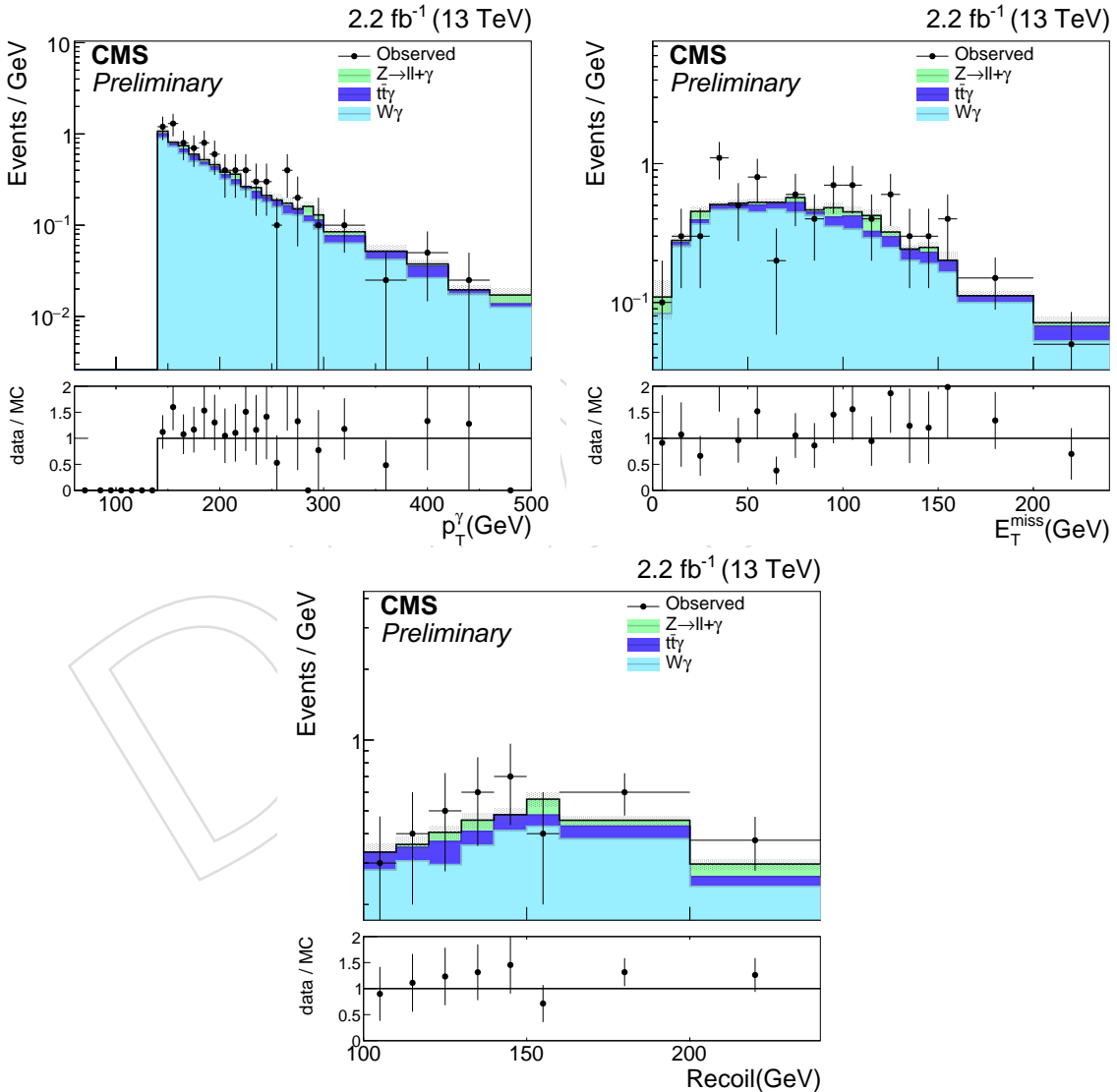


Figure 30: Distributions of  $p_T^\gamma$ ,  $E_T^{\text{miss}}$ , and  $U$  in the single-muon control region.

## 7 Acceptance and Systematics

The cross section measurement is based on the formula:



$$\sigma \times Br = \frac{N_{data} - N_{BG}}{A \times \epsilon \times L}, \quad (13)$$

where  $N_{data}$  is the observed number of events and  $N_{BG}$  is the number of estimated background events.  $A$  is the geometrical and kinematic acceptance of the selection criteria,  $\epsilon$  is the selection efficiency within the acceptance, and  $L$  is the integrated luminosity.  $Br$  is the branching ratio, which in this case is 100%. The product of  $A \times \epsilon_{MC}$  is estimated from the Monte Carlo simulation.

The product of  $A \times \epsilon_{MC}$  in the cross section calculation is determined using a MC simulated sample. The values for  $A \times \epsilon_{MC}$  are summarized in Table 13,14,15 and 16 for ADD and dark matter model respectively. Error indicates the statistical uncertainty on the estimation due to the limited size of the MC sample.

$A \times \epsilon_{MC}$	n=3	n=4	n=5	n=6	n=8
$M_D=1\text{TeV}$	$0.259 \pm 0.003$	$0.272 \pm 0.003$	$0.284 \pm 0.002$	$0.301 \pm 0.002$	$0.315 \pm 0.002$
$M_D=2\text{TeV}$	$0.312 \pm 0.002$	$0.313 \pm 0.002$	$0.321 \pm 0.002$	$0.315 \pm 0.002$	$0.325 \pm 0.002$
$M_D=3\text{TeV}$	$0.322 \pm 0.003$	$0.324 \pm 0.002$	$0.329 \pm 0.002$	$0.328 \pm 0.003$	$0.330 \pm 0.002$

Table 13:  $A \times \epsilon_{MC}$  for ADD as a function of  $M_D$  and n.

$A \times \epsilon_{MC}$	Mx=1 GeV	Mx=10 GeV	Mx=50 GeV	Mx=150 GeV	Mx=500 GeV	Mx=1000 GeV
Mv=10 GeV	$0.164 \pm 0.002$	$0.178 \pm 0.002$	$0.195 \pm 0.003$	$0.239 \pm 0.003$	$0.296 \pm 0.003$	$0.326 \pm 0.003$
Mv=15 GeV		$0.173 \pm 0.002$				
Mv=20 GeV	$0.159 \pm 0.002$					
Mv=50 GeV	$0.167 \pm 0.002$	$0.162 \pm 0.002$	$0.193 \pm 0.002$			
Mv=95 GeV			$0.180 \pm 0.002$			
Mv=100 GeV	$0.167 \pm 0.002$	$0.171 \pm 0.002$				
Mv=200 GeV	$0.189 \pm 0.002$		$0.186 \pm 0.002$	$0.231 \pm 0.002$		
Mv=295 GeV				$0.210 \pm 0.002$		
Mv=300 GeV	$0.205 \pm 0.002$		$0.209 \pm 0.002$			
Mv=500 GeV	$0.236 \pm 0.003$				$0.296 \pm 0.002$	
Mv=995 GeV						
Mv=1000 GeV	$0.275 \pm 0.003$			$0.281 \pm 0.002$		$0.331 \pm 0.003$
Mv=1995 GeV						$0.319 \pm 0.002$
Mv=2000 GeV	$0.322 \pm 0.003$				$0.320 \pm 0.002$	
Mv=10000 GeV	$0.302 \pm 0.002$	$0.302 \pm 0.002$	$0.299 \pm 0.002$	$0.298 \pm 0.003$	$0.318 \pm 0.003$	$0.336 \pm 0.003$

Table 14:  $A \times \epsilon_{MC}$  for Vector Dark Matter as a function of Mx and Mv.

$A \times \epsilon_{MC}$	Mx=1 GeV	Mx=10 GeV	Mx=50 GeV	Mx=150 GeV	Mx=500 GeV	Mx=1000 GeV
Mv=10 GeV	$0.161 \pm 0.002$		$0.208 \pm 0.002$	$0.248 \pm 0.002$	$0.307 \pm 0.002$	$0.334 \pm 0.003$
Mv=15 GeV		$0.175 \pm 0.002$				
Mv=20 GeV	$0.165 \pm 0.002$					
Mv=50 GeV	$0.165 \pm 0.002$	$0.160 \pm 0.002$	$0.203 \pm 0.003$			
Mv=95 GeV			$0.192 \pm 0.002$			
Mv=100 GeV	$0.169 \pm 0.002$	$0.169 \pm 0.002$				
Mv=200 GeV	$0.178 \pm 0.002$		$0.187 \pm 0.002$	$0.239 \pm 0.002$		
Mv=295 GeV				$0.229 \pm 0.002$		
Mv=300 GeV	$0.206 \pm 0.003$		$0.204 \pm 0.002$			
Mv=500 GeV	$0.232 \pm 0.003$			$0.236 \pm 0.003$	$0.308 \pm 0.002$	
Mv=995 GeV					$0.293 \pm 0.002$	
Mv=1000 GeV	$0.285 \pm 0.003$			$0.281 \pm 0.002$		$0.333 \pm 0.003$
Mv=1995 GeV						$0.327 \pm 0.003$
Mv=2000 GeV	$0.318 \pm 0.003$				$0.320 \pm 0.003$	
Mv=10000 GeV	$0.301 \pm 0.003$	$0.303 \pm 0.003$	$0.301 \pm 0.002$		$0.325 \pm 0.003$	$0.343 \pm 0.003$

Table 15:  $A \times \epsilon_{MC}$  for Axial Vector Dark Matter as a function of Mx and Mv.

$A \times \epsilon_{MC}$	$\Lambda=3000$ GeV
Mx=1 GeV	$0.477 \pm 0.004$
Mx=10 GeV	$0.479 \pm 0.003$
Mx=50 GeV	$0.481 \pm 0.003$
Mx=100 GeV	$0.481 \pm 0.003$
Mx=200 GeV	$0.489 \pm 0.003$
Mx=400 GeV	$0.497 \pm 0.003$
Mx=800 GeV	$0.515 \pm 0.003$
Mx=1300 GeV	$0.522 \pm 0.003$

Table 16:  $A \times \epsilon_{MC}$  for Electroweak Scalar Dark Matter as a function of Mx for  $\Lambda=3000$  GeV.

The photon energy scale, jet and  $E_T^{\text{miss}}$  energy scale and resolution, and pileup related contributions are considered as sources of systematic uncertainty in the acceptance calculation. The uncertainty on the photon energy scale is about 1.5% and met energy scales, translates into  $A \times \epsilon$  as 5%. Uncertainties on  $E_T^{\text{miss}}$  are estimated in accordance to the MET POG prescription. Contributions from the jet energy scale, jet resolution and unclustered energy scale uncertainties are accounted for in the uncertainty on the  $E_T^{\text{miss}}$ . The uncertainty on the integrated luminosity is 4.6%.

A summary of the systematic uncertainties on  $A \times \epsilon$  for different signal samples and irreducible background is shown in Table: 17

Sample	Jet energy scale [%]	Photon ES [%]
V Mx-10 Mv-10	+4.40,-3.99	+4.79,-4.18
V Mx-1000 Mv-10000	+1.51,-1.59	+1.59,-1.71
AV Mx-10 Mv-10	+4.35,-3.97	+4.55,-4.23
AV Mx-1000 Mv-10000	+1.43,-1.48	+1.54,-1.56
ADD MD-1 d-6	+2.33,-2.36	+2.43,-2.49
ADD MD-3 d-3	+2.33,-2.36	+2.43,-2.49
$Z(\rightarrow \nu\nu) + \gamma$	+4.30,-4.42	+4.49,-4.59

Table 17: Percentage systematic uncertainties in  $A \times \epsilon_{MC}$  for various signal and background sources.

A summary of the systematic uncertainties for backgrounds are shown in Table: 18

Sources	Znunugamma [%]	Wgamma [%]	Jets faking photon [%]	Electron faking photon	gamma-jet	Other bkg [%]
Luminosity	2.7	2.7	-	-	2.7	2.7
PDF and Scale	5.37	8.9	-	-	-	-
EWK corrections	11	7	-	-	-	-
Jets faking photon	-	-	30	-	-	-
Electron faking photon	-	-	-	22	-	-
gamma+jet	-	-	-	-	100	-
Jet, MET, photon energy scale	6	6	-	-	6	6
Scale Factors	6	6	-	-	6	6

Table 18: Summary of systematic uncertainties for different background sources.

## 8 Results

### 8.1 Estimates after full selection

After applying our full selection criteria, we observe 77 events in  $2.32 \text{ fb}^{-1}$  of data. Table 19 shows the estimated number of events and uncertainty from each background for the full 2015 run. The  $p_T$  spectrum and particle flow  $E_T^{\text{miss}}$  of the full combination of our selected candidate events and estimated backgrounds can be seen in Figure 31 and the  $p_T/E_T^{\text{miss}}$  and number of jets distribution is shown in Figure 32.

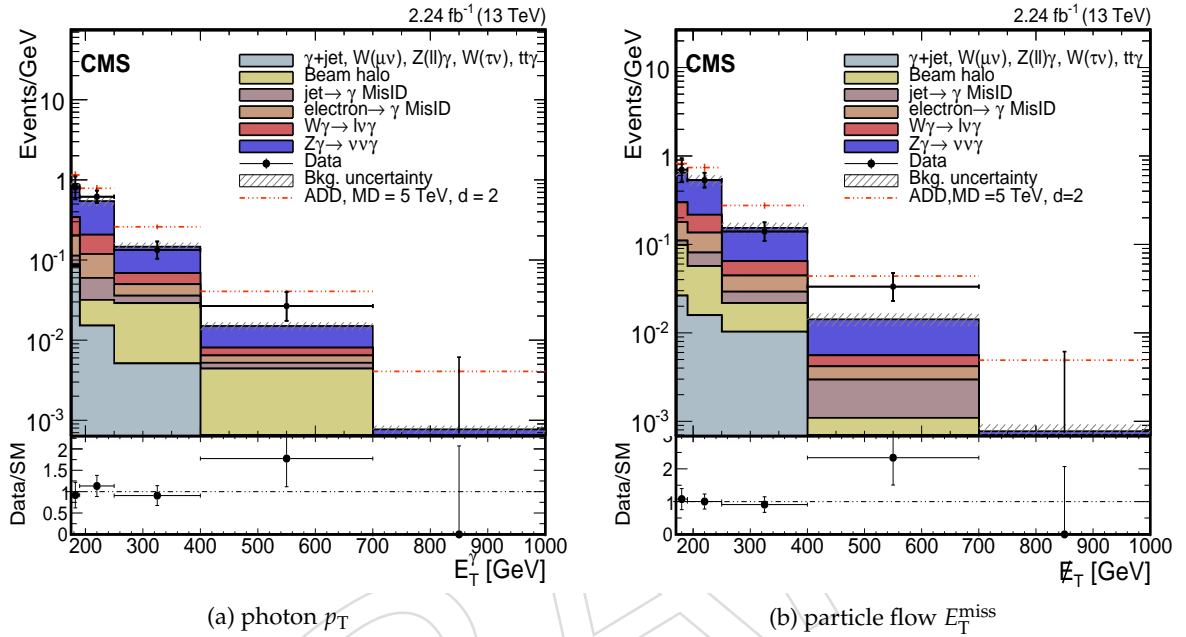


Figure 31: The photon  $p_T$  and  $E_T^{\text{miss}}$  distribution for the candidate sample, compared with estimated contributions from SM backgrounds, and background uncertainty includes statistical and systematic error.

Process	Estimate
$Z(\rightarrow \nu\bar{\nu}) + \gamma$	$42.10 \pm 6.31$
$W(\rightarrow \ell\nu) + \gamma$	$10.69 \pm 1.49$
$W \rightarrow e\nu$	$7.35 \pm 1.24$
jet $\rightarrow \gamma$ fakes	$3.36 \pm 1.13$
Beam halo	$5.90 \pm 4.70$
$tt\gamma$	$1.55 \pm 0.10$
$W\mu\nu$	$0.96 \pm 0.68$
$Z(\ell\ell)\gamma$	$0.55 \pm 0.04$
$\gamma + \text{jet}$	$0.10 \pm 0.10$
Total background	$72.4 \pm 8.21$
Data	77

Table 19: Summary of estimated backgrounds and observed total number of candidates for  $2.32 \text{ fb}^{-1}$  of 2015 data.

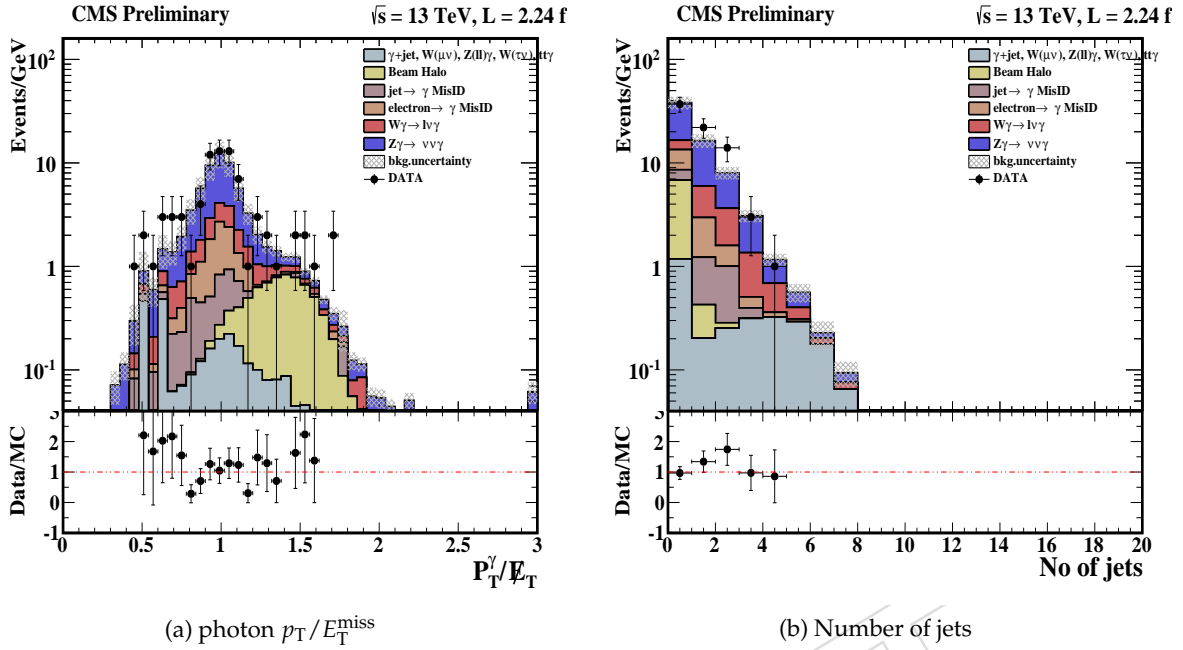


Figure 32: The photon  $p_T/E_T^{\text{miss}}$  and number of jets distribution for the candidate sample, compared with estimated contributions from SM backgrounds, and background uncertainty includes statistical and systematic error.

## 9 Interpretation

To cast the results of this analysis into statements on new physics processes, three different interpretations are performed. First is a generic, model-independent upper limit on the production cross section of (an) invisible particle(s) accompanied by a high-energy photon, as a function of the photon  $p_T$  threshold. The second is in terms of ADD bulk graviton production in association with a photon, in the plane of the two parameters of the ADD model,  $n$  and  $M_D$ . Finally, interpretation under the simplified model of dark matter production is explored, presented as cross section upper limits of vector, axial vector, and scalar mediator particles that subsequently decay to pairs of dark matter particles. Parameter space of mediator mass and dark matter mass are scanned.

### 9.1 Limits on ADD Model

We perform shape-based analysis using the the photon  $p_T$  spectrum. We adopt the official CMS statistical higgs combination tool[? ], used for upper crosssection limits.

The method adopted is  $CL_S$  [? ] and systematic uncertainties are introduced as nuisance parameters following log-normal distributions. Nuisances arising from luminosity uncertainty and scale and PDF uncertainties are mostly applied on the processes normalization, i.e. no dependency on the photon transverse energy is considered. For systematics due to jet/met energy scale, photon energy scale, EWK uncertainty, qcd background, electron faking photon background uncertainties this is not true, hence nuisances are treated differently. So for all these uncertainties, we provide shape in terms of photon  $p_T$  spectrum.

The expected and observed 95% CL limits are summarized in Table 20.

Limits on  $M_D$  are summarized in Table 21. We exclude any  $M_D$  value up to 2.65 TeV at a 95% confidence interval using LO calculation.

$\sigma$ , [fb]	n=3	n=4	n=5	n=6
$M_D=1\text{TeV}$	55.60(47.02)	54.16(44.66)	49.55 (40.19)	46.06(36.66)
$M_D=2\text{TeV}$	42.14(33.20)	42.09(33.06)	41.64(32.88)	41.12(32.45)
$M_D=3\text{TeV}$	37.64(28.89)	35.83(27.96)	35.52(27.38)	35.50(27.33)

Table 20: ADD 95%CL observed(expected) limits on the cross section as a function of  $M_D$  and  $n$  ( $p_T > 130$  GeV/c).

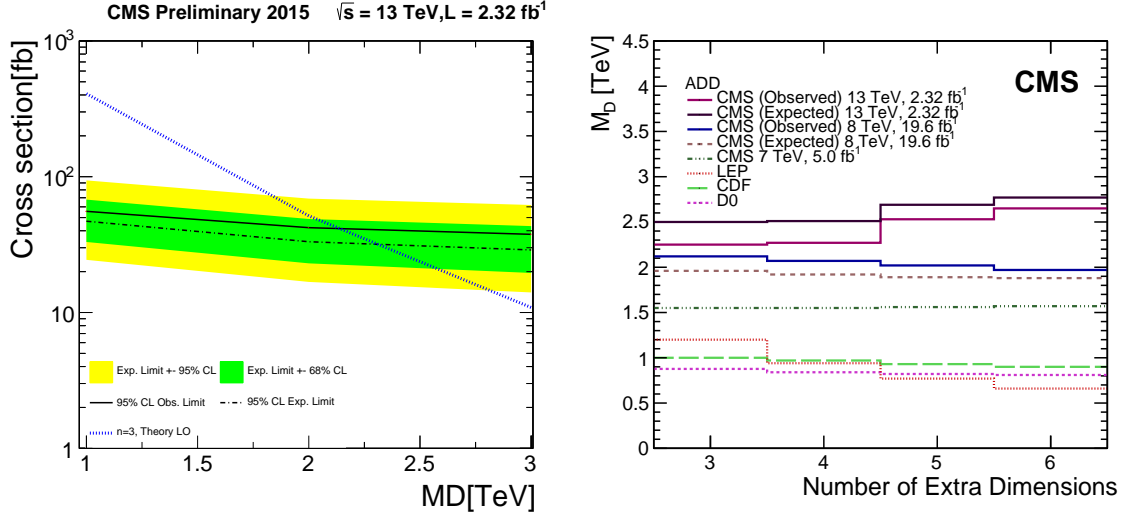


Figure 33: (a) The 95% CL upper limits on the LO ADD cross sections as a function of  $M_D$  for  $n = 4$ . (b) Limits on  $M_D$  as a function of  $n$ , compared to LO results from similar searches at the Tevatron and LEP. Also the results from the CMS 8TeV are also shown.

Fig 33 shows the limit on the cross section, along with the cross section for 3 extra dimensions as a function of  $M_D$  (left) and lower limit on  $M_D$  vs number of extra dimensions  $n$ . A comparison with the existing limits from the Tevatron and LEP is also shown .

n	Obs. Limit [TeV]	Exp. Limit, [TeV]
3	2.25	2.50
4	2.27	2.51
5	2.53	2.69
6	2.65	2.77

Table 21: 95%CL observed and expected limits on  $M_D$  as a function of  $n$

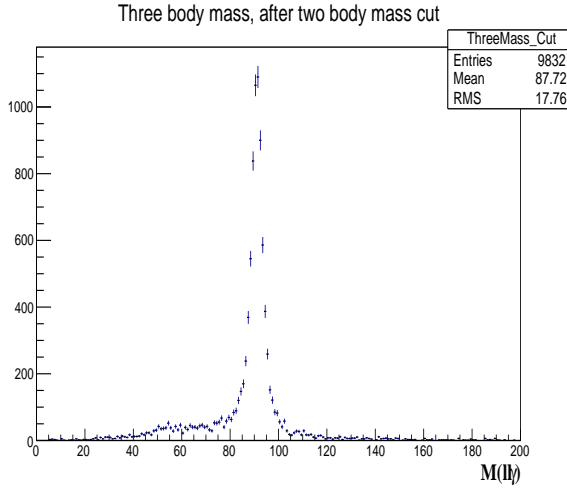


Figure 34: Invariant mass of  $Z(\mu\mu)\gamma$  system with a dimuon mass to be less than 80 GeV

## A PF Worst Charged Hadron Isolation

As mentioned in Section 3, Worst charged hadron isolation(WCHI) is defined by performing the charged hadron isolation for every vertex in the event and then we select the maximum. We need to optimize the new effective area for the same as the ones used for charged hadron isolation can have a huge pileup dependence. We consider a data sample of  $Z(\mu\mu)\gamma$  candidates. Selection Details:

- Events are selected from the 2015 DoubleMuon primary data-set.
- Require at least one photon with  $E_T > 15$  GeV in the barrel passing medium Photon ID.
- Require 2 muons with leading muon  $p_T > 20$  GeV and the trailing muon  $p_T > 10$  GeV.
- Require muons to satisfy the loose ID.
- Require 2 muons to be separated from each other by atleast  $\Delta R > 1.0$ .

To select radiative decays, require dimuon mass to be less than 80 GeV. We then select events with this criteria with three body mass between 80-100 for efficiency studies.

Figure ?? represents the three body mass with a dimuon mass to be less than 80 GeV.

We can assess if there is a pileup dependence if we use the default effective area for WCHI and same threshold for the cut as used in charged hadron isolation. Figure 35 represents the WCHI ; 1.37 (where 1.37 is the recommended cut for charged hadron isolation) efficiency as a function of photon eta and rho. And one can see there is a huge pileup dependence. So we do need to optimize the Effective area.

### A.1 Finding the correct EA

We look at 2 bins in photon eta for the barrel case i.e  $|\eta| < 1.0$  and  $1.5 < |\eta| < 1.0$ . And then look at the profile plot of WCHI as a function of rho for both of these cases and fit in the range where we see good statistics . Once we get the EA, we repeat the efficiency study with this new effective area.

Figure 36 shows the rho distribution for the 2 eta bins and Figure 37 shows the profile plots for the WCHI as a function of rho. We perform fitting between rho values 3 to 15 for  $|\eta| < 1.0$  and

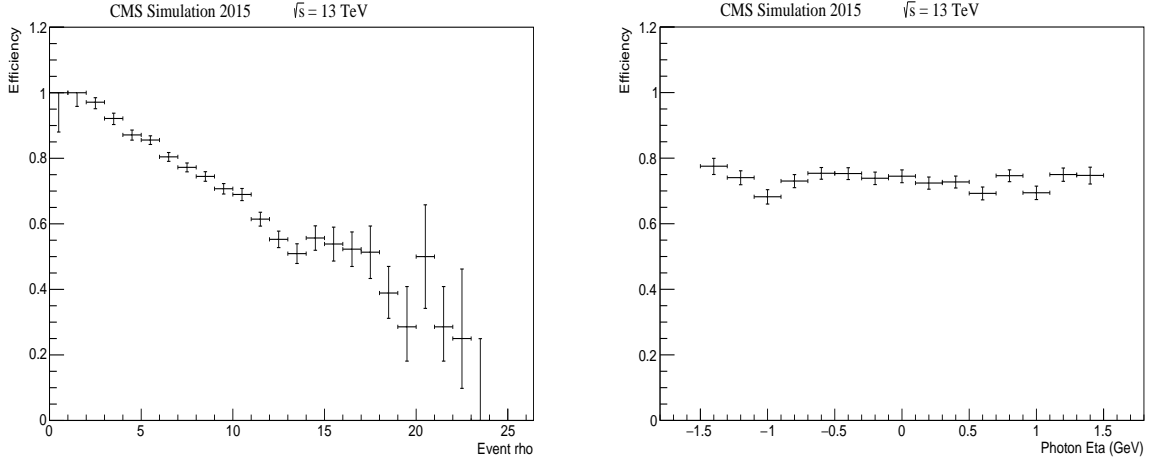


Figure 35: WCHI cut efficiency as a function of rho and photon eta

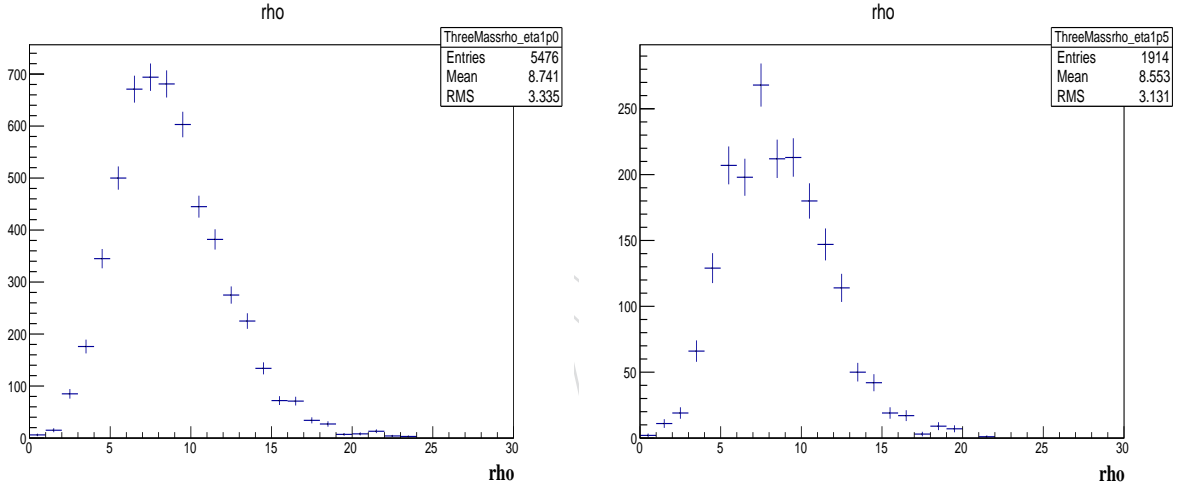


Figure 36: Rho distribution for 2 eta bins,  $|\eta| < 1.0$  (left) and  $1.5 < |\eta| < 1.0$  (right)

812 then between rho values 3 to 12 for  $1.5 < |\eta| < 1.0$ . Slope of these fits gives new EA, i.e EA1=  
813 0.078 and EA2= 0.089 for  $|\eta| < 1.0$  and  $1.5 < |\eta| < 1.0$  respectively.

814 Figure 38 left plot shows the efficiency as a function of WCHI cut value and it is 90% we cut  
815 at 1.37 (which is default charged hadron isolation cut value). We choose this cut value for our  
816 studies.

817 Also the right plot shows the efficiency of WCHI  $\geq 1.37$  (with new EA) as a function of rho, and  
818 we can see there is no pileup dependence in the region where we did the fit.

## 819 B Optimization of MET cut

820 We optimized the MET cut based on  $S/\sqrt{B}$ , where we considered ADD as one of the signal  
821 model. Table 22 refers to the signal and total backgrounds estimate for varying the MET cut  
822 from 140 GeV to 180 GeV in steps of 10 GeV. And one can see MET  $> 170$  GeV gives the best  
823 significance. This study was performed before we introduced the PF Worst charged hadron  
824 isolation cut, but that cut wouldn't change the conclusion.



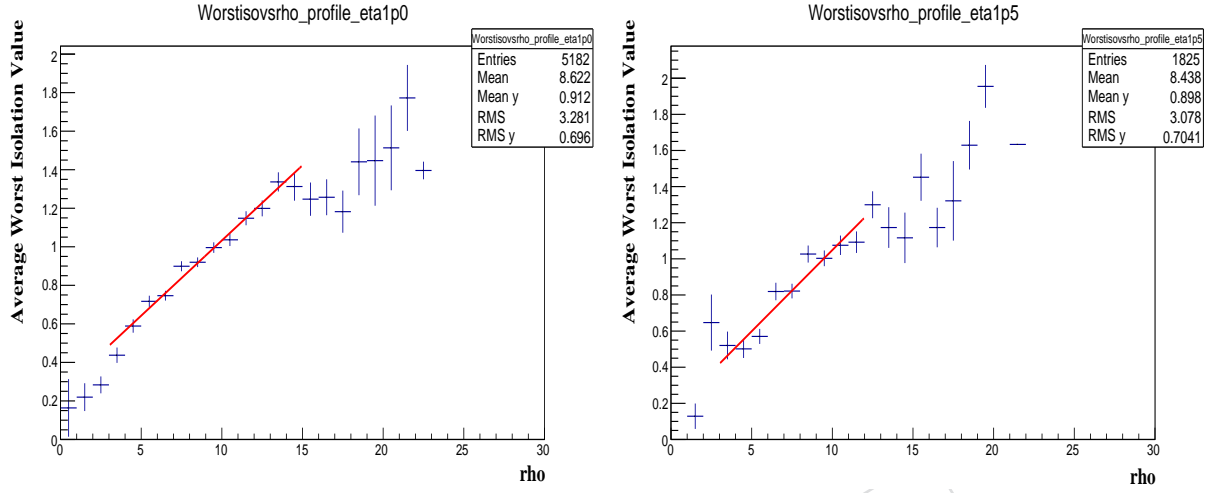


Figure 37: Profile plots for 2 eta bins,  $|\eta| < 1.0$  (left) and  $1.5 < |\eta| < 1.0$  (right)

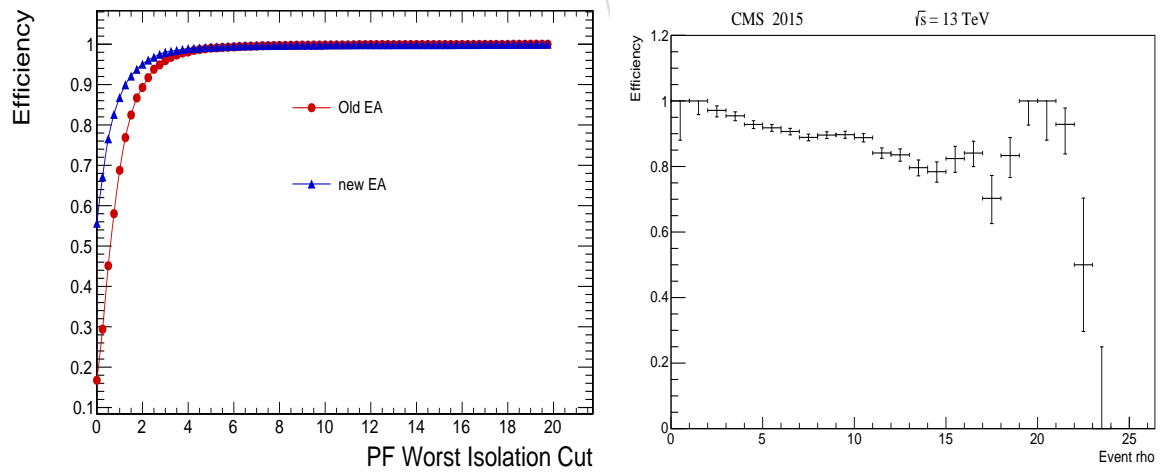


Figure 38: Profile plots for 2 eta bins,  $|\eta| < 1.0$  (left) and  $1.5 < |\eta| < 1.0$  (right)

Process	MET > 140	MET > 150	MET > 160	MET > 170	MET > 180
$Z(\rightarrow \nu\bar{\nu}) + \gamma$	$58.9 \pm 6.3$	$57.1 \pm 6.1$	$54.7 \pm 5.8$	$51.6 \pm 5.5$	$47.9 \pm 5.1$
$W(\rightarrow \ell\nu) + \gamma$	$15.8 \pm 1.8$	$14.3 \pm 1.6$	$13.0 \pm 1.5$	$11.7 \pm 1.3$	$10.3 \pm 1.2$
$W \rightarrow e\nu$	$14.8 \pm 1.3$	$14.4 \pm 1.2$	$13.9 \pm 1.2$	$13.0 \pm 1.1$	$12.1 \pm 1.1$
jet $\rightarrow \gamma$ fakes	$4.7 \pm 1.5$	$4.6 \pm 1.5$	$4.3 \pm 1.4$	$4.0 \pm 1.3$	$3.9 \pm 1.3$
Beam halo	$3.11 \pm 3.94$	$3.11 \pm 3.94$	$3.11 \pm 3.94$	$3.11 \pm 3.94$	$3.11 \pm 3.94$
Zllgamma	$0.86 \pm 0.05$	$0.79 \pm 0.05$	$0.72 \pm 0.05$	$0.63 \pm 0.04$	$0.55 \pm 0.04$
Wmunu	$0.95 \pm 0.06$	$0.95 \pm 0.06$	$0.95 \pm 0.06$	$0.95 \pm 0.06$	$0.95 \pm 0.06$
Gamma+jets	$1.08 \pm 0.68$	$0.76 \pm 0.66$	$0.11 \pm 0.11$	$0.11 \pm 0.11$	$0.0 \pm 0.0$
Total background	$100.3 \pm 7.9$	$96.1 \pm 7.7$	$90.8 \pm 7.4$	$85.1 \pm 7.1$	$78.9 \pm 6.8$
Data	113	105	101	92	84
Signal ADD MD2d5	$51.7 \pm 4.1$	$51.1 \pm 4.1$	$50.3 \pm 4.0$	$49.1 \pm 3.9 \pm 47.5 \pm 3.8$	
$S/\sqrt{B}$	4.19	4.21	4.23	4.24	4.23

Table 22: Summary of estimated backgrounds and observed total number of candidates for 2.24 fb<sup>-1</sup> of 2015 data for variations of MET cut

## References

- [1] N. Arkani-Hamed, S. Dimopoulos, G. Dvali, “The Hierarchy Problem and New Dimensions at Millimeter”, [arXiv:9803315](#).
- [2] D. Abercrombie et al., “Dark Matter Benchmark Models for Early LHC Run-2 Searches: Report of the ATLAS/CMS Dark Matter Forum”, [arXiv:1507.00966](#).
- [3] H.-L. Lai et al., “Uncertainty induced by QCD coupling in the CTEQ global analysis of parton distributions”, *Phys. Rev. D* **82** (2010) 054021, doi:10.1103/PhysRevD.82.054021, [arXiv:1004.4624](#).
- [4] GEANT4 Collaboration, “GEANT4: A Simulation toolkit”, *Nucl. Instrum. Meth. A* **506** (2003) 250, doi:10.1016/S0168-9002(03)01368-8.
- [5] <https://twiki.cern.ch/twiki/bin/view/CMS/CutBasedPhotonID2012>.
- [6] G. Bozzi et al., “Production of Drell-Yan lepton pairs in hadron collisions: Transverse-momentum resummation at next-to-next-to-leading logarithmic accuracy”, *Phys. Lett. B* **696** (2011) 207–213, doi:10.1016/j.physletb.2010.12.024, [arXiv:1007.2351](#).
- [7] A. Denner, S. Dittmaier, M. Hecht, and C. Pasold, “NLO QCD and electroweak corrections to W+ $\gamma$  production with leptonic W-boson decays”, *JHEP* **04** (2015) 018, doi:10.1007/JHEP04(2015)018, [arXiv:1412.7421](#).
- [8] A. Denner, S. Dittmaier, M. Hecht, and C. Pasold, “NLO QCD and electroweak corrections to Z +  $\gamma$  production with leptonic Z-boson decays”, *JHEP* **02** (2016) 057, doi:10.1007/JHEP02(2016)057, [arXiv:1510.08742](#).
- [9] C. Collaboration, “Search for supersymmetry in pp collision events at  $\sqrt{s} = 8$  TeV with a photon, lepton, and missing transverse energy”, CMS Note 2006/076, 2014.